BRNO UNIVERSITY OF TECHNOLOGY
VYSOKÉ UČENÍ TECHNICKÉ V BRNĚ

FACULTY OF MECHANICAL ENGINEERING
FAKULTA STROJNÍHO INŽENÝRSTVÍ

INSTITUTE OF AEROSPACE ENGINEERING
LETECKÝ ÚSTAV

NUMERICAL ANALYSIS OF BIO-MIMETIC CONCEPT FOR ACTIVE FLOW CONTROL ON WING SURFACE
NUMERICKÁ ANALÝZA BIO-MIMETICKÉHO KONCEPTU ŘÍZENÍ PROUDU NA POVRCHU KŘÍDLA

MASTER'S THESIS
DIPLOMOVÁ PRÁCE

AUTHOR — **Bc. Jakub Čermák**
AUTOR PRÁCE

SUPERVISOR — **Ing. Robert Popela, Ph.D.**
VEDOUCÍ PRÁCE

BRNO 2016

VYSOKÉ UČENÍ TECHNICKÉ V BRNĚ
FAKULTA STROJNÍHO INŽENÝRSTVÍ

Zadání diplomové práce

Ústav:	Letecký ústav
Student:	**Bc. Jakub Čermák**
Studijní program:	Strojní inženýrství
Studijní obor:	Stavba letadel
Vedoucí práce:	**Ing. Robert Popela, Ph.D.**
Akademický rok:	2016/17

Ředitel ústavu Vám v souladu se zákonem č.111/1998 o vysokých školách a se Studijním a zkušebním řádem VUT v Brně určuje následující téma diplomové práce:

Numerická analýza bio-mimetického konceptu řízení proudu na povrchu křídla

Stručná charakteristika problematiky úkolu:

Bio-mimetické principy jsou v posledních letech studovány jako další možnost zvýšení aerodynamické účinnosti těles v proudu vzduchu. Bylo prokázáno, že významně umožňují rozšířit obálku režimů práce např. u profilů. Cílem práce je ověření možností zvýšení kritického úhlu náběhu a maximálního vztlaku u profilů pomocí flexibilních ploch v zadní části profilu na horním povrchu a to s využitím CFD prostředků.

Cíle diplomové práce:

Vytvoření CFD modelu profilu a následně segmentu křídla s flexibilními ploškami na horním povrchu. Simulace změn aerodynamických charakteristik v závislosti na výchylce plošek a analýza potřebné tuhosti plošek pro automatickou funkci bez dodávky energie.

Seznam literatury:

CHOI, H., PAPR, H., SAGONG, W., LEE, S., Biomimetic flow control based on morphological features of living creatures, Physics of Fluids, 24, 121302 (2012).

Termín odevzdání diplomové práce je stanoven časovým plánem akademického roku 2016/17

V Brně, dne

L. S.

doc. Ing. Jaroslav Juračka, Ph.D. ředitel ústavu	doc. Ing. Jaroslav Katolický, Ph.D. děkan fakulty

ABSTRACT

In this paper optimization on airfoil equipped with upper-side elastic flap is carried out. The optimization process is done by using of URANS CFD method. In first chapters the history of development of wing with movable flaps is briefly described. The paper continues with description and motivation on choice of computational method. Geometry and mesh generation is briefly explained. Verification and validation of computational method is also presented. The actual case study is focused on airfoil LS(1)-0417mod equipped with 20%, 30% and 40% long rigid flap on various angles of attack. The aerodynamic performance of each case is discussed together with the flow-field analysis. The non-linear structural analysis using FEM software is carried out in order to evaluate elastic flap bending stiffness and deformed shape to fulfil self-adaptive requirements.

KEYWORDS

Active flow control, aerodynamics, ANSYS, biomimetics, CFD, elastic flap, FEM, Fluent, passive flow control, rigid flap, structural analysis, URANS

ABSTRAKT

V této diplomové práci je provedena optimalizace profilu křídla vybaveného elastickou klapkou umístěnou na horní straně profilu. Optimalizační proces je proveden s vyžitím CFD prostředků, konkrétně URANS metody. V prvních kapitolách je popsána historie vývoje křídla vybaveného pohyblivými klapkami. Práce pokračuje popisem a zdůvodněním volby numerické metody. Vytvoření geometrie a výpočetní sítě je krátce popsáno. V práci je také prezentována validace a verifikace dané výpočetní metody. Případová studie je zaměřena na profil LS(1)-0417mod vybavený 20%, 30% a 40% dlouhou, pevnou kalpkou na různých úhlech náběhu. Aerodynamická účinnost společně s proudovým polem je analyzována. Je provedena nelineární pevnostní analýza s využitím MKP programu za účelem vyhodnocení ohybové tuhosti a deformovaného tvaru elastické klapky tak, aby byly splněný podmínky nutné pro automatické vychýlení.

KLÍČOVÁ SLOVA

Aktivní řízení proudu, aerodynamika, ANSYS, biomimetika, CFD, elastická klapka, Fluent, MKP, pasivní řízení proudu, pevná klapka, pevnostní analýza, URANS

ČERMÁK, Jakub *Numerical analysis of bio-mimetic concept for active flow control on wing surface*: master's thesis. Brno: Brno University of Technology, Faculty of Mechanical Engineering, Institute of Aerospace Engineering, 2017. 85 p. Supervised by Ing. Robert Popela, Ph.D.

DECLARATION

I declare that I have elaborated my master's thesis on the theme of "Numerical analysis of bio-mimetic concept for active flow control on wing surface" independently, under the supervision of the master's thesis supervisor and with the use of technical literature and other sources of information which are all quoted in the thesis and detailed in the list of literature at the end of the thesis.

Brno ....

(author's signature)

First, I would like to thank to my supervisor for valuable feedback and guidance through writing this paper. Also, I would like to thank to my girlfriend and whole family who supported me during whole studying process. Thanks go also to my colleagues at work for encouragement and technical support.

CONTENTS

List of symbols, physical constants and abbreviations **11**

1 Introduction **13**
1.1 Self Actuating Flaps 13

2 Theoretical Background **15**
2.1 Self-Adaptive Flaps Principle 15
2.1.1 Flap Position 15
2.1.2 Flap Length 16
2.1.3 Flap Deflection 16
2.2 Airfoil Choice 16

3 Computational Method **19**
3.1 Geometry Set-up 19
3.2 Computational Mesh 20
3.2.1 Grid Type 20
3.2.2 Near-wall Treatment 22
3.3 Simulation Settings 23
3.3.1 Input variables 23
3.3.2 Solver Setting 24
3.3.3 Boundary Conditions 26
3.3.4 Convergence 27
3.3.5 Test Run 28

4 Validation & Verification **31**
4.1 Mesh Independence Study 31
4.2 Convergence Issues 33
4.3 Validation 34

5 Numerical Study of Flapped Airfoil **37**
5.1 Objectives 37
5.2 Simulation Set-up 37
5.2.1 Geometry 37
5.2.2 Cases Assessment 38
5.2.3 Computational Grid 39
5.2.4 Transient Simulation Set-up 40

6 Case Results **45**
6.1 Flow Analysis . . . 45
6.1.1 1^{st} Phase . . . 45
6.1.2 2^{nd} Phase . . . 45
6.1.3 3^{rd} Phase . . . 47
6.2 Results Comparison . . . 48
6.2.1 20% Flap Cases . . . 48
6.2.2 30% Flap Cases . . . 49
6.2.3 40% Flap Cases . . . 50
6.3 Discussion . . . 51
6.4 Solution Evaluation & Accuracy . . . 52

7 Structural Analysis **53**
7.1 Load Distribution . . . 53
7.2 Computational Model . . . 54
7.3 Finite Element Method . . . 54
7.3.1 Validation . . . 55
7.3.2 Structural Analysis of Elastic Flap . . . 56

8 Final Assesment **59**

9 Concluding Remarks **61**

Bibliography **63**

List of appendices **71**

A Mesh Independence Study **73**

B Flow Analysis **77**

C Case Results **79**
C.1 F_80_20 Case . . . 79
C.2 F_70_30 Case . . . 81
C.3 F_60_40 Case . . . 83

D Structural Analysis **85**

LIST OF SYMBOLS, PHYSICAL CONSTANTS AND ABBREVIATIONS

$a_{0m,ISA}$	Speed of sound defined at 0m ISA $[ms^{-1}]$
c	Airfoil chord length $[m]$
c_d	Drag coefficient of the airfoil $[-]$
c_f	Friction coefficient of the airfoil $[-]$
c_l	Lift coefficient of the airfoil $[-]$
c_m	Moment coefficient of the airfoil $[-]$
d	Domain diameter $[m]$
EI	Flexural rigidity (bending stiffness) $[Nm^2]$
l_f	Flap length [%]
l_p	Flap position [%]
M_∞	Free-stream Mach number $[-]$
p_0	Total pressure $[Pa]$
p_d	Dynamic pressure $[Pa]$
p_s	Static pressure $[Pa]$
Re	Reynolds number $[-]$
Re_x	Reynolds number defined at the x-position $[-]$
T_{ft}	Flow-through time $[s]$
t_{BL}	Boundary layer thickness $[m]$
t_f	Flap thickness [%]
u_*	Friction velocity $[ms^{-1}]$
U_∞	Free-stream velocity $[ms^{-1}]$
w	Displacement of the tip of the elastic flap $[m]$
w_{mod}	Displacement of the tip of the rigid flap $[m]$

w_{val_num}	Measured displacement in validation study $[m]$
w_{val_exp}	Measured displacement in experiment $[m]$
y^+	Non-dimensional wall distance $[-]$
y_0	First layer height $[m]$
Δt	Time-step size $[s]$
δ	Flap deflection $[deg]$
Δx	Mesh element size $[m]$
μ	Dynamic viscosity $[kgm^{-1}s^{-1}]$
ρ	Density $[kgm^{-3}]$
σ_o	Bending stress $[MPa]$
τ_ω	Friction stress $[Pa]$
AoA	Angle of Attack
BL	Boundary Layer
CFL	Courant-Friedrichs-Lewy number
DES	Detached Eddy Simulation
FEM	Finite Element Method
ISA	International Standard Atmosphere
LES	Large Eddy Simulation
MIS	Mesh Independence Study
NITA	Non-Iterative Time Advancement
RANS	Reynolds-Averaged Navier-Stokes
SST	Shear Stress Transport
TKE	Turbulent Kinetic Energy
URANS	Unsteady Reynolds-Averaged Navier-Stokes

1 INTRODUCTION

Biomimetics can be simply describe as a *"scientific discipline of implementing nature-based ideas to engineering systems"* [1]. By this approach many of man-made inventions were further innovated often with exceptional results. By the means of the flow control inspiration in the nature is rather appealing. An aircraft's wing can serve as a very good example. The *Alula* which denotes the first group of two to six feathers on the bird's wings was observed to be deployed when landing. As a result, slats can be now found on the majority of big commercial aircraft enabling the airplane to fly at higher angles of attack by delaying flow separation on the surface. The principle of the slats development is demonstrated in the Figure 1.1.

Fig. 1.1: Leading edge slats as observed on the bird's wings [2].

The flow control can be divided according to the initial impulse as a *passive* and *active*. The passive flow control simply reacts in accordance with the actual flow condition with no power input whereas the active flow control is denoted to be one with sensors and certain power input to optimally react to the flow condition. This paper deals with one of the birds phenomena: self-activated movable flaps or the so-called pop-up feathers [1].

1.1 Self Actuating Flaps

The history behind the development of these pop-up flaps came from 1930s. Aerospace engineer Wolfgang Liebe first observed pop-up motion of the upper feathers on crows during landing. This behaviour was also observed during manoeuvres requiring higher angle of attack and on different kinds of birds i.e. Seagulls as shown in following Figure 1.2. Thus, this behaviour was considered as a high-lift feature. Later, Liebe also carried out experimental study involving strip of leather attached to the upper side of one wing of the Messerschmitt BF 109. Unfortunately this caused asymmetrical distribution of the lift force and the project was cancelled [3] [4].

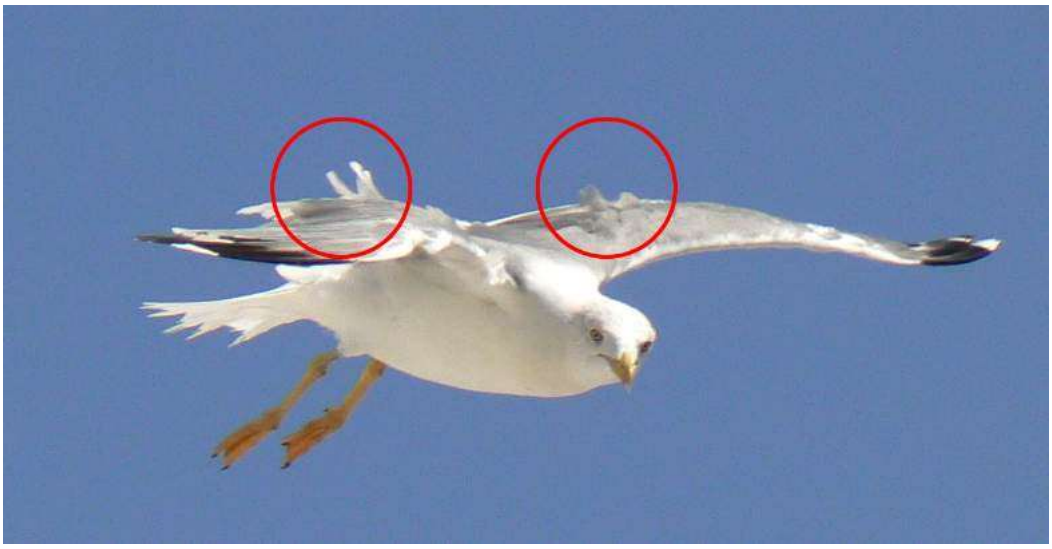

Fig. 1.2: Slow approach by the Seagull with extended upper flaps.

Since then, many other studies on self-adaptive movable flaps were carried out. Especially the experimental work of *D.W. Bechert et al.* from German Aerospace Center (DLR) proved the idea of the self-adaptive flaps to be very promising. Their application of plastics strips on the glider plane STEMME S10 and further flight tests showed exceptional results with maximum lift coefficient gain of 11%! Other papers present studies focused on different position, size, materials and for different Reynolds numbers. However, these publications often show inconsistent results. For example, the work of Kernstine [5] dealing with the position and size concluded that the ideal position of the movable flaps lies in frontal part of the airfoil. In contrast, the paper presented by Bechert [3] recommends the position of the flaps near the trailing edge. There are also other studies dealing with the oscillation of the upper flaps followed by vortex shedding and its benefit to the overall airfoil performance. As a conclusion, the amount of published papers and results variations suggest this phenomenon to be further investigated. In case of this paper the study is focused on the numerical analysis of the airfoil used in General Aviation LS(1)-0417mod equipped with the rigid and flexible movable flaps on the upper surface [3] [5] [6].

2 THEORETICAL BACKGROUND

Since the actual knowledge of the flow-field and the principle of the mechanism is required for the correct numerical simulation theoretical analysis based on published papers is carried out.

2.1 Self-Adaptive Flaps Principle

The original idea how the flaps work come from W. Liebe. He claimed that the separation region, which is coming from the trailing edge, is bound by the presence of the elevated flap. The flap itself is popped up by the reverse flow condition. Basically, the purpose of the flaps is to stop recirculation region spreading out towards the leading edge. Therefore, the flaps were named as a **Reverse Flow Bags**. The mechanism is visualized by the following Figure 2.1 [3].

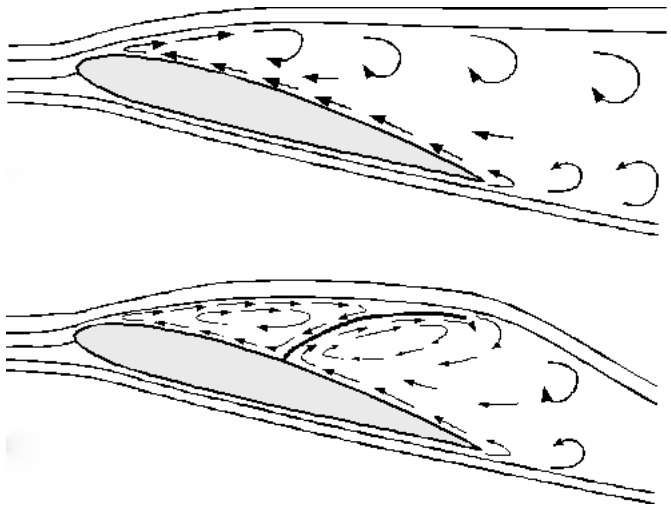

Fig. 2.1: Mechanism of the "Reverse Flow Bags"[7].

Ideally, the flap stays attached during flight with low angle of attack. When the reverse flow starts to appear flap would gradually lift off and prevent further recirculation propagation. By this acting, the big increment in lift and delay of the flow separation can be achieved.

2.1.1 Flap Position

According to the Bechert [3] the flap should be located in 60-70% of the chord. However, this presumption is based on the fact that the used airfoil is laminar so it is predicted that the flow stays attached with the laminar boundary layer for

the most of the upper surface. Bechert also recommend to position the flap slightly upstream (approx. ≥ 1 % of chord) otherwise the flap cannot response properly [3] [4].

2.1.2 Flap Length

The flap length directly influences the lift coefficient. According to Bechert, longer flaps cause bigger increment in lift. However, with longer flaps the problem with reattachment of the flap and with the flexibility arises. One solution can be using more smaller flaps which according to the reference [6] looks promising.

2.1.3 Flap Deflection

The self-adaptive flap is deflected in respect to the actual flow condition. It does not protrude to the high-speed region which would cause spoiler-like effect. The flap would be also ineffective when slightly elevated allowing the further spreading of the recirculation region. According to the numerical study presented in reference [4] and [8] the self-adaptive flap does not give the optimal deflection angle causing largest gain in lift. The largest increment in lift is when the flap is slightly touching the separated shear layer as shown in the Figure 2.2 [4] [8].

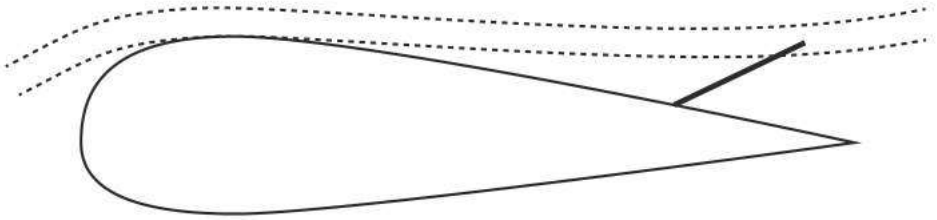

Fig. 2.2: The flap protruding to the separated shear layer denotes high efficiency of the mechanism.

2.2 Airfoil Choice

The airfoil chosen for this study came from the family of airfoils designated for General Aviation. Such an airfoil was developed in the 1973 by using the subsonic viscous computer code which resulted in the 17-percent-thick **GA(W)-1** airfoil. In development, emphasis was placed especially on good lift-to-drag ratio at $c_l = 1.0$ and high maximum lift coefficient of about 2.0 at a Reynolds number of $6 \cdot 10^6$. That

was achieved by some of the features such as:

Large leading edge radius to diminish the peak of the leading edge pressure and thus delay the flow separation

Blunt trailing edge for moderating the upper surface pressure recovery

Contoured shape from the reason of the uniform chord-wise pressure distribution

Also, 13-percent-thick **GA(W)-2** airfoil was generated as a result of the flight tests [9] [10].

The development of before-mentioned airfoils gave rise to creation of new airfoil family with various thickness and shape according to their purpose. Two branches of this family are named in the form: LS(1) (low-speed, first series) and MS(1) (medium-speed, first series). The following two digits denote the design lift coefficient in tenths and the other two digits denote the actual thickness in chord percentage. By this rule the GA(W)-1 airofil becomes **LS(1)-0417** and analogically the GA(W)-2 becomes **LS(1)-0413**. Further modificated airfoils were given the 'mod' suffix. The development is illustrated in the Figure 2.3 [10].

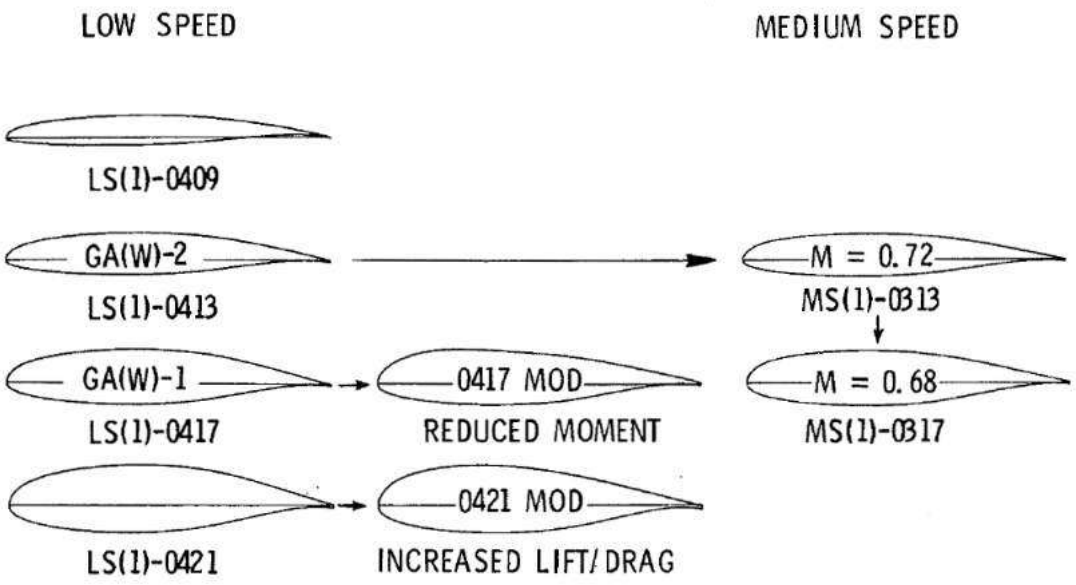

Fig. 2.3: Development of the General Aviation airfoil family [10].

The airfoils were further modificated in order to enhance the aerodynamic performance. In the case of the LS(1)-0417 the airfoil was reshaped to give better performance during climb and to reduce the pitching moment. The modification resulted in the LS(1)-0417mod airfoil. The redesigned shape and its consequence is shown in the following Figure 2.4.

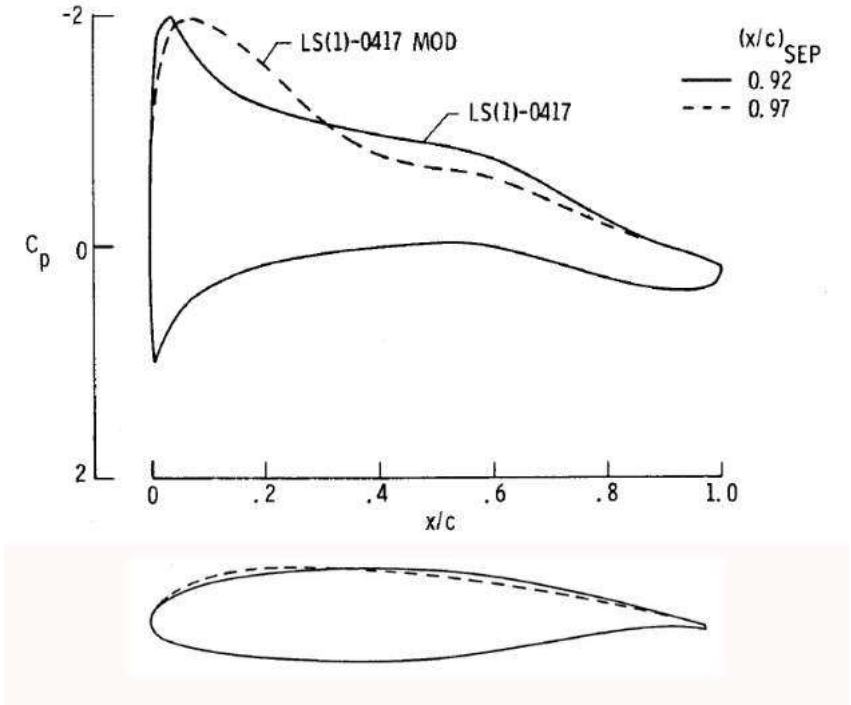

Fig. 2.4: LS(1) - 0417mod airfoil and its performance at M = 0.15, Re = $4 \cdot 10^6$ and $c_l = 1.0$ [10].

The modification caused reduction in the pressure gradient as can be spotted in the Figure 2.4. The flat pressure distribution on the upper side located approximately in the middle of the chord has a major influence on the stall behaviour. This reduced pressure gradient retards the forward movement of the separation causing delay of stall and more docile behaviour of airfoil during stall. This behaviour is favourable for the purposes of this thesis so the **LS(1)-0417mod** airfoil was chosen for further analysis with the movable flaps [10].

3 COMPUTATIONAL METHOD

For the purposes of this thesis the ANSYS computational software package was utilized. In the term of meshing the ICEM v14.5 was implemented and as the solver the Fluent v14.5 was used. Geometry was created and edited using the Catia V5 software. All the calculations were performed by using the server cluster provided by the Institute of Aerospace Engineering of the Faculty of Mechanical Engineering in Brno.

3.1 Geometry Set-up

As previously stated, the airfoil LS(1)-0417mod was chosen for the analysis. The airfoil data were obtained from the UIUC database [11]. Cloud of points was imported to the CAD software and connected by default spline in the default XY plane. The origin of the coordinate system was placed in the 25% of the chord to address the aerodynamic centre with the X-axis in the direction of the flow. Two furthermost points of the airfoil were connected with a straight line to create a blunt trailing edge which is more convenient in the terms of hexa mesh generation. The chord length was set to be 1 meter.

The computational domain was closed by the C-type border which was again chosen for simpler meshing. However, this choice was overridden by further discovery which led to the use of conventional O-Grid type of domain. The overall look is shown in the figure 3.1 together with the detail of the blunt trailing edge. The diameter of the domain will be later discussed in the Verification chapter.

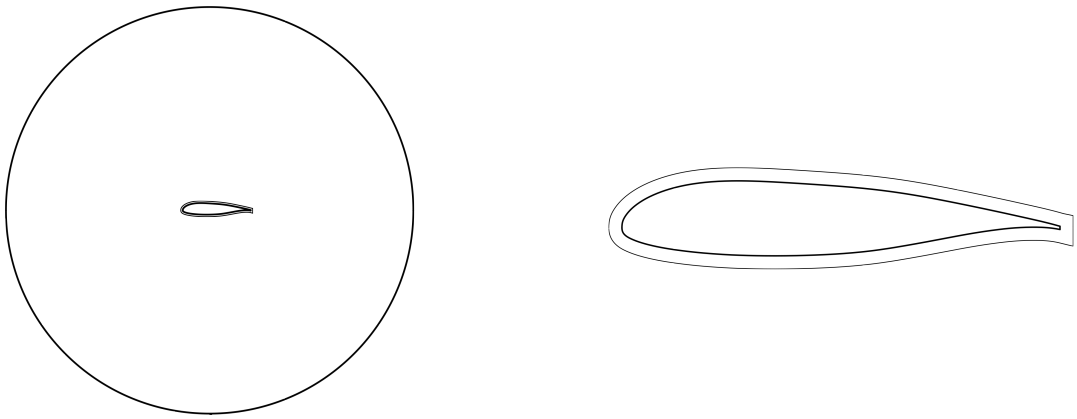

(a) Domain boundaries. (b) Detail of the LS(1)-0417mod airfoil.

Fig. 3.1: Input computational geometry.

3.2 Computational Mesh

The creation of geometry is followed by the mesh generation which is necessary for computational fluid analysis. This step is critical for overall solution since the quality and type of computational mesh directly affect the actual numerical calculations and may lead to incorrect and faulty results.

3.2.1 Grid Type

When creating a 2-dimensional mesh two main ways are taken in to account. Structured and unstructured computational meshes are options for numerical study each with its pros and cons [12] [13] [14].

- **Structured grid** The conformal map is used in order to fit the geometry by creating curvilinear grid. In 2D, quadrilateral cells are used for building these type of grid. Beside its good performance on filling the space (less cells required) there are also some drawbacks:
  - \+ Usually better convergence
  - – Rather difficult and time consuming generation
  - – Limited on more complex geometries
  - – Possible numerical diffusion if the flow is not aligned with the cells
- **Unstructured grid** Unstructured grid is equipped with no conformal map. Therefore, the connectivity between cells is maintained by the connectivity table which describes connectivity for each element. From this reason, no restriction is applied to cell type choice. In 2D, usually triangular elements are used.
  - \+ Little building time
  - \+ Easy concentration where necessary
  - – More time-expensive and memory-expensive
  - – Sensitivity to CAD geometry imperfections

As previously mentioned, this task of simulating flow over the airfoil led the author to generate typical structured C-Grid made entirely from quadrilateral elements. This type of mesh undertake the whole mesh independence study. However, as was later discovered, the mesh generation for the case of airfoil equipped with flap was almost impossible. This problem raised due to the complexity of the airfoil shape such as high-angled sharp corners. Further explanation is presented in following chapters. From this reason, the author decided to create so-called **hybrid mesh** which, as the name suggest, is the combination of different type of elements in the same domain. This special type of unstructured grid combines the pros of the structured and unstructured grid. Here, it allows to use quadrilateral cells in near-

wall region to provide better resolution of viscous effects and triangular elements elsewhere in order to efficiently fill up the rest of the domain. Such a case is shown in the figure 3.4 [12].

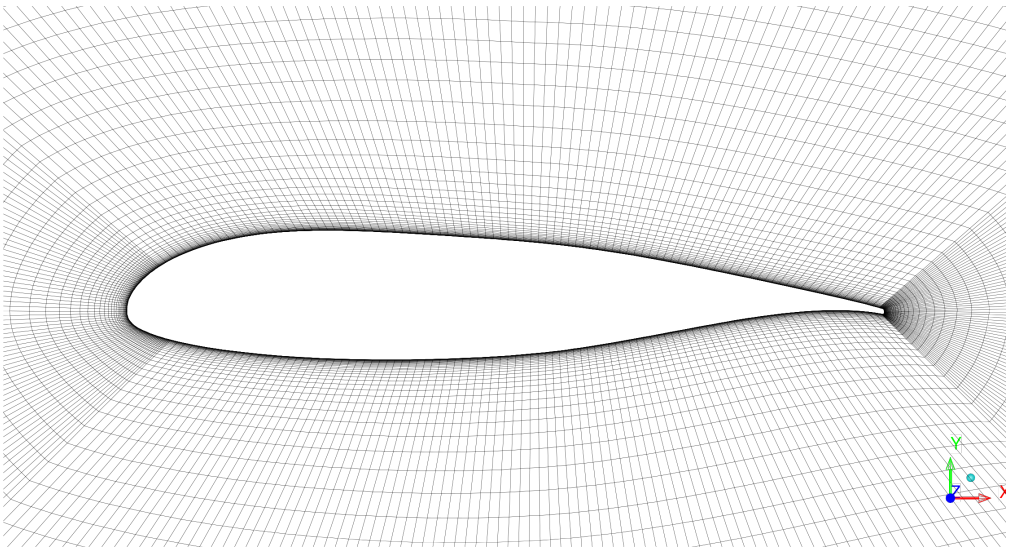

Fig. 3.2: Example of structured mesh constructed of quadrilateral cells

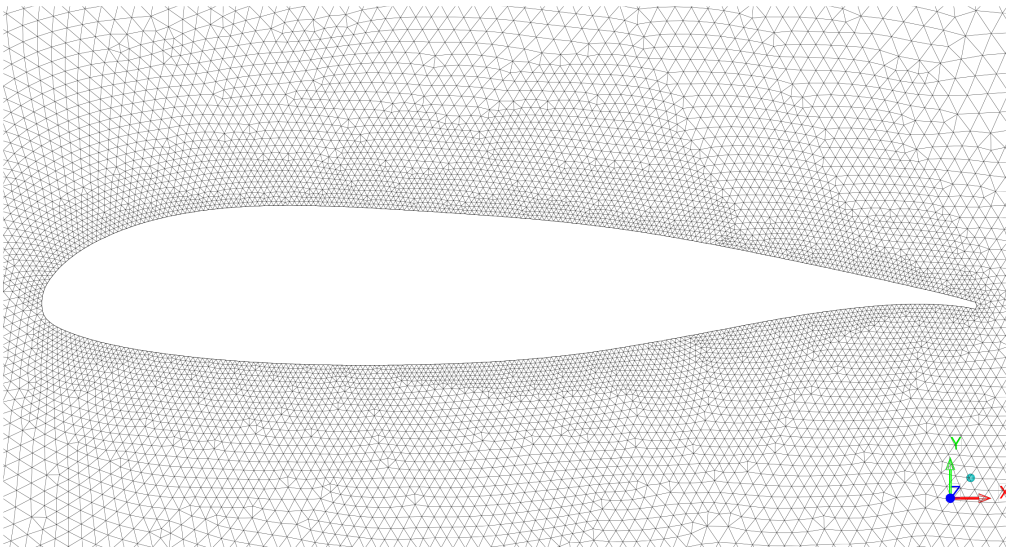

Fig. 3.3: Example of unstructured mesh with triangular elements.

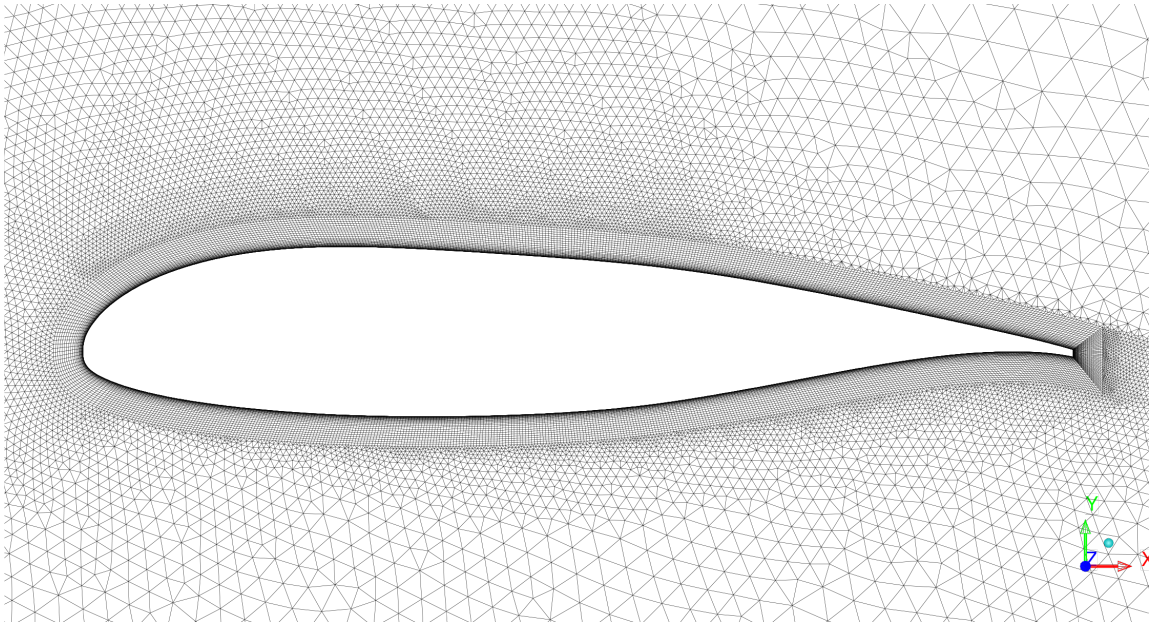

Fig. 3.4: Hybrid mesh used for validation with quad and tri zone.

3.2.2 Near-wall Treatment

Other very important feature of the mesh is its wall treatment and appropriate resolution. One must consider that the near-wall treatment determines the boundary layer behaviour and linked flow separation which is critical for the results credibility.

To predict the flow separation as accurately as possible the boundary layer will be fully resolved. To achieve this goal several conditions must be met.

The first one is to fulfil the condition regarding the first layer height defined as:

$$y^+ \approx 1\,[-] \tag{3.1}$$

where the y^+ stands for non-dimensional wall distance. By taking this into account the formula for determining the first layer height can be used [15]:

$$y_0 = \frac{y^+ \mu}{\rho u_*}\,[m] \tag{3.2}$$

where the μ represents the dynamic viscosity and ρ stands for the density of the fluid. Symbol u_* represents the friction velocity which is calculated as:

$$u_* = \sqrt{\frac{\tau_\omega}{\rho}} = \sqrt{\frac{\frac{1}{2} c_f \rho U_\infty^2}{\rho}}\,\left[ms^{-1}\right] \tag{3.3}$$

where τ_ω is a wall shear stress, c_f is a stress coefficient and U_∞ represents the free-stream velocity. For a turbulent boundary layer there is several options for approximating the shear stress coefficient. The one chosen for this case is Schlichting skin-friction correlation defined as [15]:

$$c_f = [2log_{10}(Re_x) - 0.65]^{-2.3}\,[-] \tag{3.4}$$

where Re_x stands for the Reynolds number defined at x position. By introducing variables defined in the section 3.3 the first layer height is evaluated as:

$$y_0 = \frac{1 \cdot 1.7894 \cdot 10^{-5}}{1.225 \cdot 0.6321} = 2,31 \cdot 10^{-5}\,[m]$$

Between other conditions required for proper boundary layer resolution belongs requirement regarding the number of cells. The rule of thumb says that in the boundary layer there should be placed about 10-15 layers of a growth ratio no more than 1.3 [16] [20]. The height of the boundary layer must be estimated as well. The turbulent boundary layer height on the flat plate can be derived by using the Blasius equation. Then, the thickness can be expressed as [18]:

$$t_{BL} = 0.37\frac{x}{\sqrt[5]{Re_x}} = 0.37\frac{c}{\sqrt[5]{Re}} = 0.37\frac{1}{\sqrt[5]{1000000}} = 0.023\,[m] \tag{3.5}$$

To introduce some assurance, the value is rounded up as follows:

$$t_{BL} \approx 0,03\,[m] \tag{3.6}$$

This offset curve is evident in the input geometry in the Figure 3.1b creating imaginary BL border.

Fulfilling before-mentioned conditions not always promises well resolved boundary layer. The visual inspection of a converged solution must be done and when unsatisfactory, further re-meshing is unavoidable.

3.3 Simulation Settings

In this chapter, overall solver setting is described together with the boundary conditions and discretization method.

3.3.1 Input variables

The simulation was set up with following parameters. Reynolds number used for calculation was chosen in respect to provided data for the tested airfoil . Also, to properly simulate low speed application the value was chosen as a [17]:

$$Re = 1000000\,[-]$$

By introducing variable obtained for 0 meter ISA condition the desired value of the free-stream velocity can be establish as [18]:

$$U_\infty = \frac{Re \cdot \mu}{\rho \cdot c}\,[ms^{-1}] \tag{3.7}$$

By substituting variables in before-mentioned formula the free-stream velocity can be expressed. Values used for calculation are presented in the following table 3.1:

Variable	Value	Unit
ρ	1.225	[kgm^{-3}]
Re	1000000	[-]
μ	$1.79 \cdot 10^{-5}$	[kgs$^{-1}m^{-1}$]
c	1	[m]
U_∞	**14.607**	[ms^{-1}]

Tab. 3.1: Input variables used for calculation.

3.3.2 Solver Setting

The following parameters were used as an input to the Fluent software. Motivation to this choice is described below.

General	
Solver type	Pressure-Based
Time	Steady
Models	
Model	k-ωSST
Materials	
Fluid	Air
Solid	Aluminium
Solution methods	
Scheme	SIMPLE
Gradient	Least Squares Cell Based
Pressure	Second Order
Momentum	Second Order Upwind
TKE	Second Order Upwind
Specific Dissipation Rate	Second Order Upwind

Tab. 3.2: Solver setting.

In the Fluent software, first choice that has to be made is related to the type of solver. The **pressure-based** solver was chosen in respect to the actual flow conditions. The Mach number of the flow is calculated using the 0m ISA values as [18]:

$$M_\infty = \frac{U_\infty}{a_{0m,ISA}} = \frac{14.607}{340.2} = 0.043\,[-] \tag{3.8}$$

According to the Fluent User Guide [19] the compressibility effect are negligible at Mach number much less than the value of 1.0. This condition is more than satisfied in the studied flow. In the term of time-discretization time-averaged steady-state **RANS** model was chosen. RANS type of solution is very widely spread and used in many engineering application. Between its major advantages belongs the overall robustness, low computational cost and acceptable accuracy . On the other side the time-averaged model can not handle massive swirls and vortices [12] [19].

From the available RANS models the **SST k-ω** was chosen. The Menter's SST k-ω model came from the original Wilcox k-ω model. He noted that the standard k-ϵ is very well handling the free-stream flow whereas in the near-wall flow its performance

is very poor (in the case of adverse pressure gradient). On the other hand, the standard Wilcox k-ω suffered from excessive sensitivity to the free-stream flow but the performance in the near-wall region was superior. Menter suggest a hybrid model that is using k-ω model in the near-wall region which is transformed through blending function in to the k-ϵ model in the fully turbulent region far from the wall. The developed SST k-ω is a two-equation model with two calculated variables: k which is the turbulence kinetic energy and ω which represents the turbulence frequency or the rate of dissipation of the eddies. The model is also y^+ insensitive which means that the solution is not excessively sensitive to the value of y^+. However, to achieve best results the condition 3.1 must be met. In conclusion, the SST k-ω RANS model is nowadays most widely used across the engineering applications due to its performance and accuracy so it also promises somewhat valid results in the case of studied phenomena of upper-surface flaps [12] [19] [20].

By the means of the type of algorithm the **Pressure-Velocity Coupling Method SIMPLE** was chosen. Its major advantage to the conventional segregated algorithm is that the momentum equations and the pressure-based continuity equation are solved simultaneously. This radically improves the convergence rate but in the same time increases the memory requirement. The SIMPLE algorithm is set by default and provides iterative solution of the discretised momentum equations by using the guessed pressure field followed by pressure correction [12] [19] [20].

In the terms of spatial discretization the minimum requirement for the **Second Order** method was placed. Generally, while the first order of discretization gives better convergence the second order gives more accurate results [19] [20].

As a fluid the **Air** material with constant density and viscosity was assigned. The fluid parameters are given in the table 3.1. As a wall material the default aluminium was chosen.

3.3.3 Boundary Conditions

Choosing right boundary conditions is another critical part that directly affect the solution. In the case of this study four zones are assigned to the boundary conditions:

Outer domain border On this boundary the flow is entering and also exiting the domain. In most similar aerodynamic problems this border is assigned to the *pressure far-field* boundary which, in this case, is more than suitable. However, this condition is more suited to the compressible flow cases with higher Mach number. This boundary type with the density based solver was also tested for the studied case but the solution was unable to converge. The author headed for the *velocity-inlet* BC which is compatible with current solver setting. Although

the velocity-inlet is primary inlet condition by certain circumstances it can act also like exit-boundary. According to the Fluent User Guide the only condition for this application is that the overall continuity must be maintained. While this condition, in studied case, is fulfilled attention must be paid to the possible non-physical behaviour [19].

Inner domain border To appropriately model the airfoil boundaries the no-slip *wall* boundary condition is assigned to the inner domain boundaries.

Domain surface The filled domain is assigned to the *fluid* or *interior* type of BC.

Other geometry inside the domain Other geometry represented by the density box and the boundary layer border is assigned to the *interior* type of BC.

The location of boundary conditions is demonstrated in the following figure 3.5:

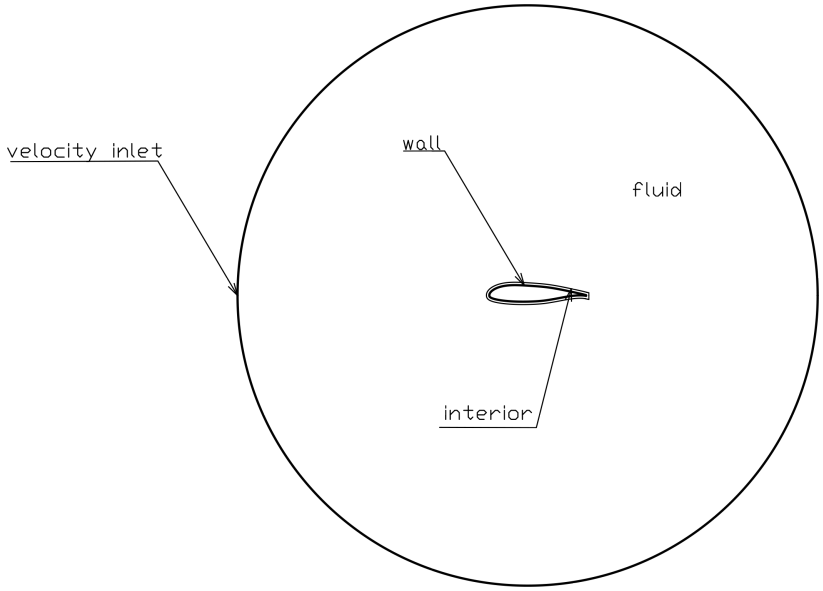

Fig. 3.5: Boundary condition distribution.

3.3.4 Convergence

The solution is monitored during the whole calculation process. For the steady-state calculations the convergence criterion is given by the means of residuals level and state of the monitors. So the first condition is related to the accuracy of the solution e.g. the residual value which should be lower than the order of $1 \cdot 10^{-3}$. Other condition is even more important. Beside the residuals level, three variables are monitored: lift coefficient, drag coefficient and moment coefficient. These variables are very much related to our problem. While they are levelled out and the residuals condition is fulfilled the solution can be proclaimed as converged. The exampled of converged steady solution is given below in the figure 3.6.

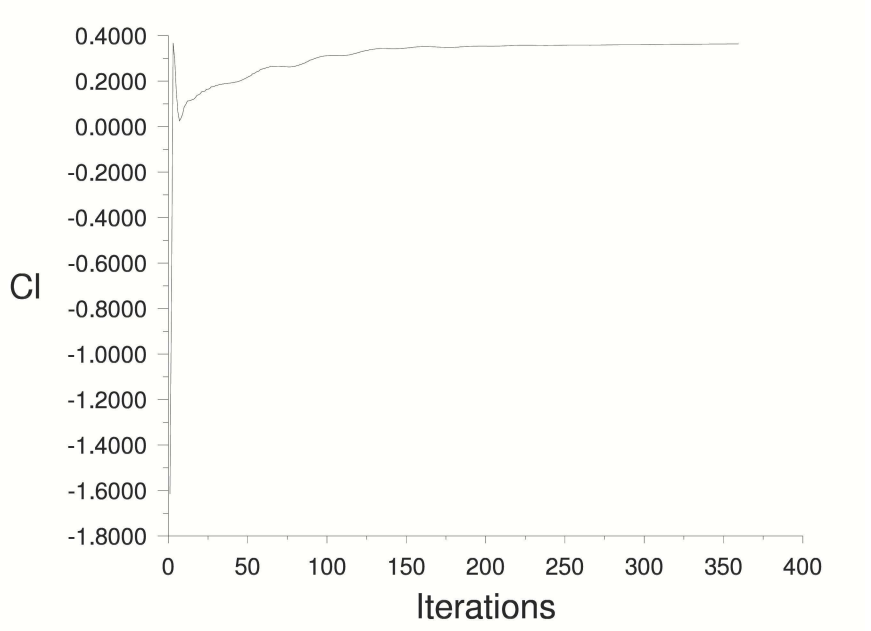

Fig. 3.6: Example of convergence progress on lift coefficient monitor.

Sometimes, when reaching convergence criterions is more difficult, lowering of under-relaxation factors was done in order to stabilise solution.

3.3.5 Test Run

In order to verify before mentioned assumptions few test runs must be performed. The goal is to validate presumptions about the boundary layer settings, convergence rate, simulation stability and visually check the flow for any non-physical behaviour. The test run was carried out on the clean airfoil which is then used for the mesh sensitivity study.

Boundary Layer Treatment

As mentioned before, in order to properly resolve the boundary layer the variable y^+ should be around the value of 1.0. The following figure 3.7 is showing the y^+ distribution on the airfoil boundary (upper and lower surface):

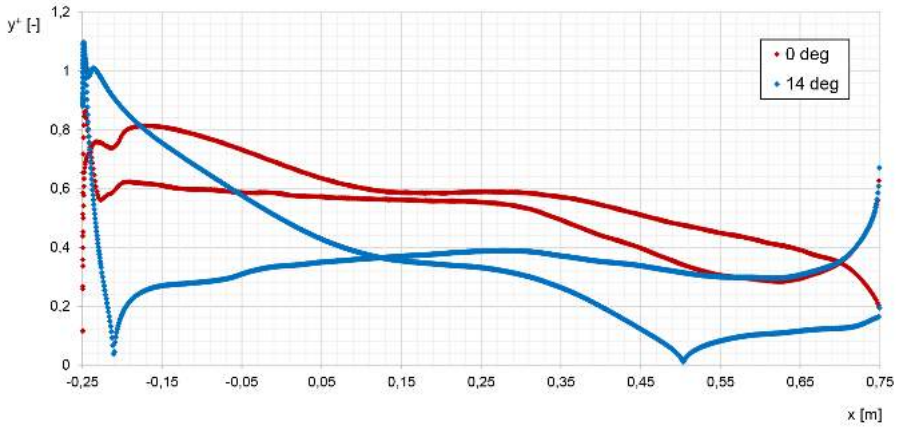

Fig. 3.7: Wall y^+ distribution on different angles of attack.

The figure shows the importance of checking the value y^+ on different angles of attack. This is due to the fact that the y^+ is related to the skin friction coefficient which is changing on different flow conditions. In this case, the mesh resolution is fulfilling (in the direction of the normal to the wall) the condition given by the formula 3.1.

Also, the estimated BL thickness should be visually checked. Using the contours the eddy viscosity ratio can be visualized. According to the [16] and [22] the higher magnitude of the eddy viscosity ratio should lie somewhere in the middle of the estimated BL. After checking contours on the airfoil on zero angle of attack it can be easily said that the the thickness of the quad region is more than sufficient. The results are showed in the following pictures 3.8:

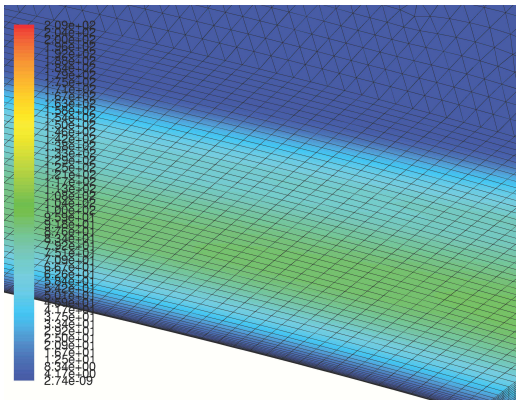

(a) Eddy viscosity ratio distribution in quad layer in the aft part of the airfoil.

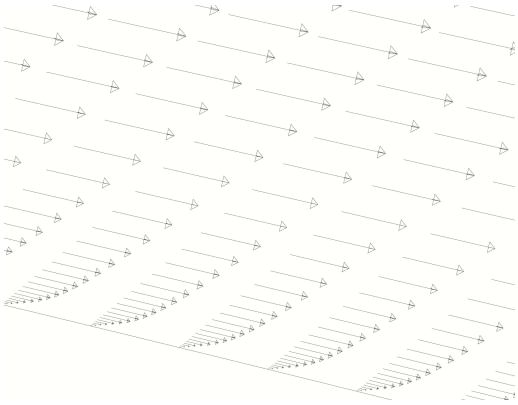

(b) Detail of the resolved boundary layer.

Fig. 3.8: Boundary layer validation.

Convergence & Visual Inspection

Convergence rate was also checked for any unexpected behaviour. The convergence rate was satisfactory, the solution converged on several thousands of iterations (mesh size of 300 000 cells). Also, the proximity of the airofil and the velocity-inlet boundary was visually inspected by using the velocity and pressure contours tab for any non-physical behaviour. The inspection proved the good applicability of beforementioned solution set-up.

4 VALIDATION & VERIFICATION

The definition can be expressed according to the [12] as follows:

Verification is a process of quantifying errors. Usually, this is done by the means of the mesh independence study which determines whether the mesh is sufficiently fine and the computation domain big enough.

Validation is a process of determining the level of representation accuracy from the perspective of the intended uses of used model. This is done by the means of the comparison with results of similar case provided by the NASA.

4.1 Mesh Independence Study

The computational domain together with the grid was created in accordance with the statements in previous chapter. The MIS was performed by the means of mesh resolution. The rough mesh was gradually refined in the proximity of the airfoil by introducing density box with higher mesh resolution (visible in the figure 3.5). Its purpose is to capture wake on higher angles of attack and connected gradients in the pressure field. In the rest of the domain, the rule of thumb says that the biggest element in the domain should not be larger than the studied body [16]. Due to this, mesh resolution on the inlet boundary condition was preserved due to whole MIS process and the rest of the domain was filled with triangles with prescribed growth ratio. Together with the resolution on different location the mesh quality is also reported. As a criterion, the cell *skewness* describing the cell distortion ranging from one (ideal quality) to zero (bad quality) was introduced. Also, to account different cell shape universal *quality* criterion was implemented. This criterion compute the aspect ratio on tri cells and determinant on the quad cells. As in the case of skewness, the quality ranges from one (ideal quality) to zero (bad quality) [21].

The MIS was performed on different angles of attack corresponding to the higher values, close to stall of the airfoil. This was done in order to account the most dramatic flow-field conditions with big wake and pressure gradients. Monitored values of lift, drag and moment coefficient were chosen in order to appropriately quantify the resulting differences.

The single grid characteristics are presented in the Appendix in the table A.1 and table A.2. The graphical results on AoA of 14deg are presented bellow in the figure 4.1:

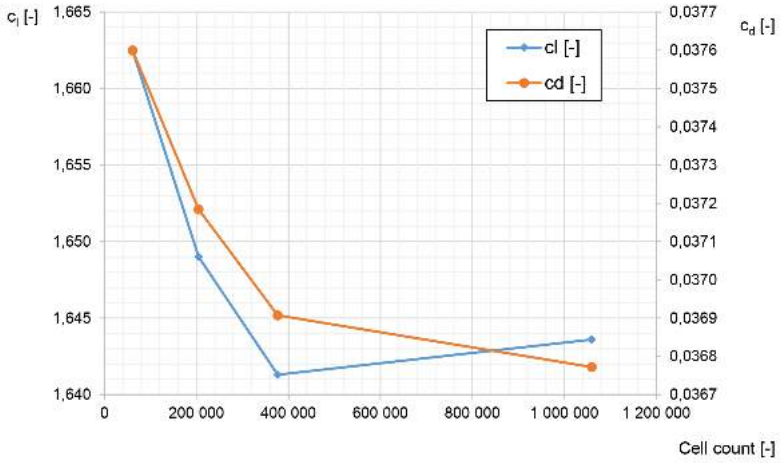

(a) Lift and drag coefficient vs. the number of cells.

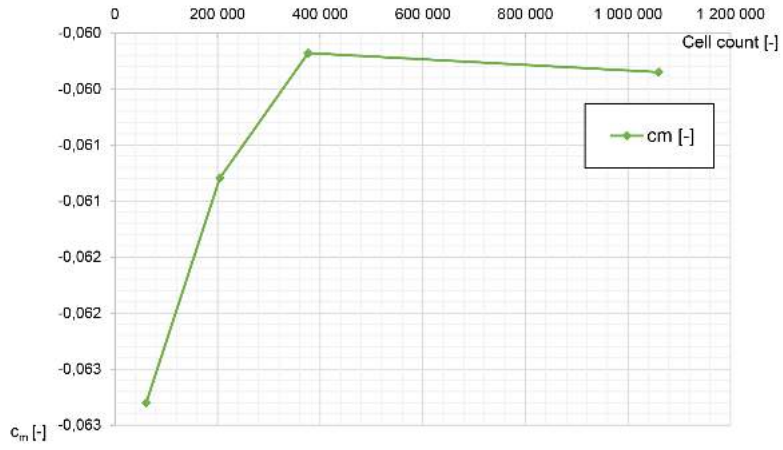

(b) Moment coefficient vs. the number of cells.

Fig. 4.1: Monitored variables of mesh independence study.

The single values and percentage difference is listed in the table 4.1:

Variable	Mesh 1	Mesh 2	Mesh 3	Mesh 4
c_l [-]	1,663	1,649	1,641	1,644
c_d [-]	0,038	0,037	0,037	0,037
c_m [-]	-0,063	-0,061	-0,060	-0,060
Difference				
Δc_l [%]	N/A	0,8	0,5	0,1
Δc_d [%]	N/A	1,1	0,7	0,4
Δc_m [%]	N/A	3,2	1,8	0,3

Tab. 4.1: Mesh independence study data.

The goal here is to have sufficiently low difference between results from two different meshes. The rule of thumb says that the difference should be lower than 5% [16]. In this case it was also aimed on the same order which is fulfilled in the difference between Mesh 3 and 4. From this it can be drawn that the **mesh 3** is mesh independent since the monitored values are no longer changing with increasing cell count.

4.2 Convergence Issues

When conducting the MIS on meshes with higher resolution issue related to the convergence arised. On higher angles of attack, especially 14deg to 16deg the solution was very hard to converge. Sometimes, even reducing under-relaxation factor did not helped and the solution cannot be reached with sufficient accuracy. Author is well aware of the inability of RANS handling stronger vortices but the difficulties even on lower angles of attack were baffling. The visual inspection of the flow-field was done by plotting the turbulent viscosity ratio and mass imbalance residuals . In the figure 4.2a the viscosity ratio influenced by the wake reached the velocity-inlet boundary. The consequence is shown in the next picture 4.2b. The residuals show instabilities causing convergence troubles. To overcome this, new computational Mesh 5 was built using the parameters proven by MIS but with bigger domain radius of 50 meters. By implementing this, the convergence issues disappeared and the solution showed much more stable convergence rate.

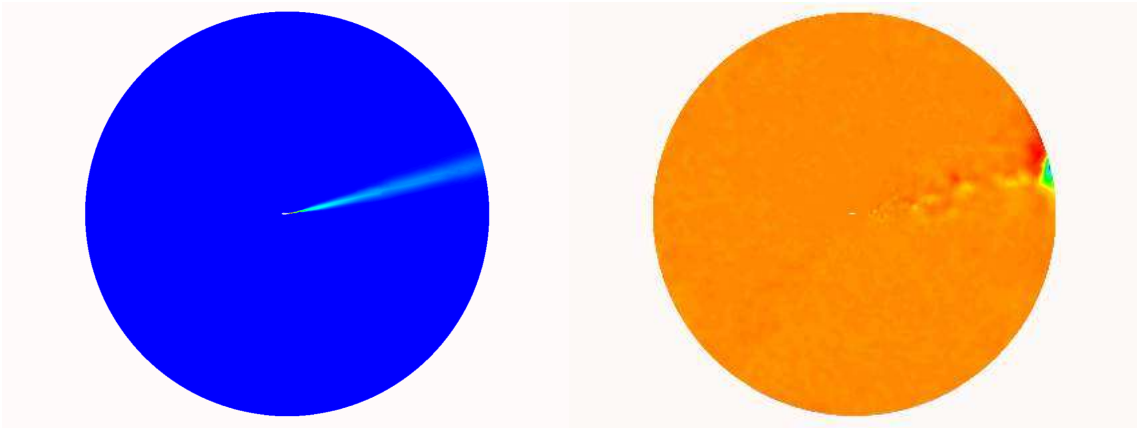

(a) Contours of viscosity ratio. (b) Contours of residuals.

Fig. 4.2: Convergence issues.

The resized mesh also undertake MIS process but presumingly showed almost similar result as independent Mesh 3. The only difference was the cell count which

increased up to 461 866 cells. All the data gathered for the purpose of MIS are presented in the section Appendix A.

4.3 Validation

To verify that the solver set-up and the mesh generation was performed well the comparison with measured data is carried out. The experimental data were gathered with the use of wind-tunnel experiments by NASA [17]. Presented data for lift, drag and moment coefficient were digitalized and used for validation of studied problem.

The solver was set up based on findings in previous chapters. The independent mesh with the radius of 50m was utilized. The simulation was performed on various angles of attack ranging from -5deg to 16deg. Further study on angles of attack after the stall was not performed due to the strong vortices formation and solver's inability to properly simulate flow field.

The comparison graphs were completed by adding the results from the free XFLR 5 software which is using well-known XFOIL solver. Comparison is carried out by visualising the lift curve, moment curve and aerodynamic polar curve. Results are showed below in the figure 4.3, 4.4 and 4.5:

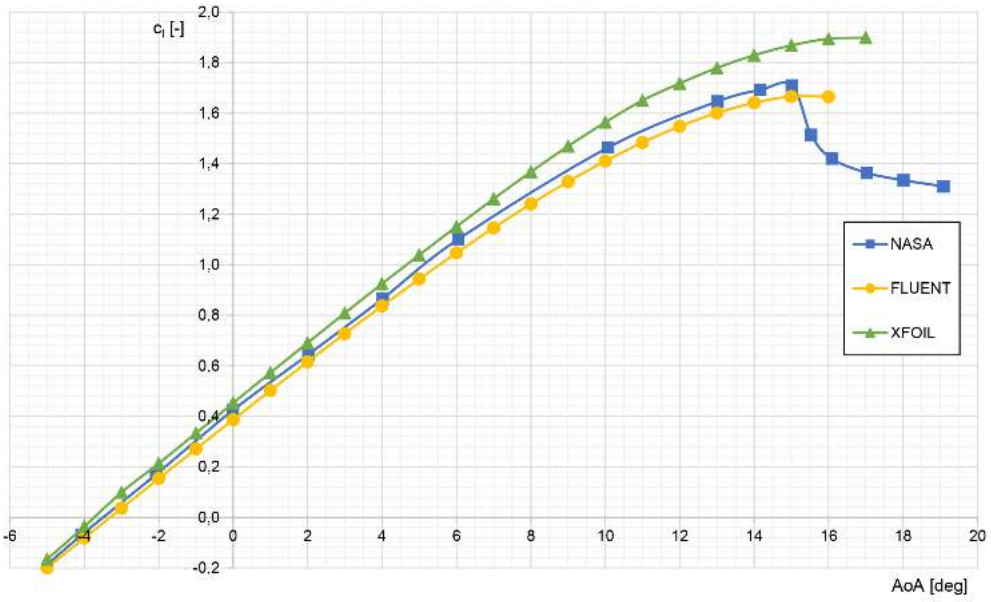

Fig. 4.3: Validation: lift curve.

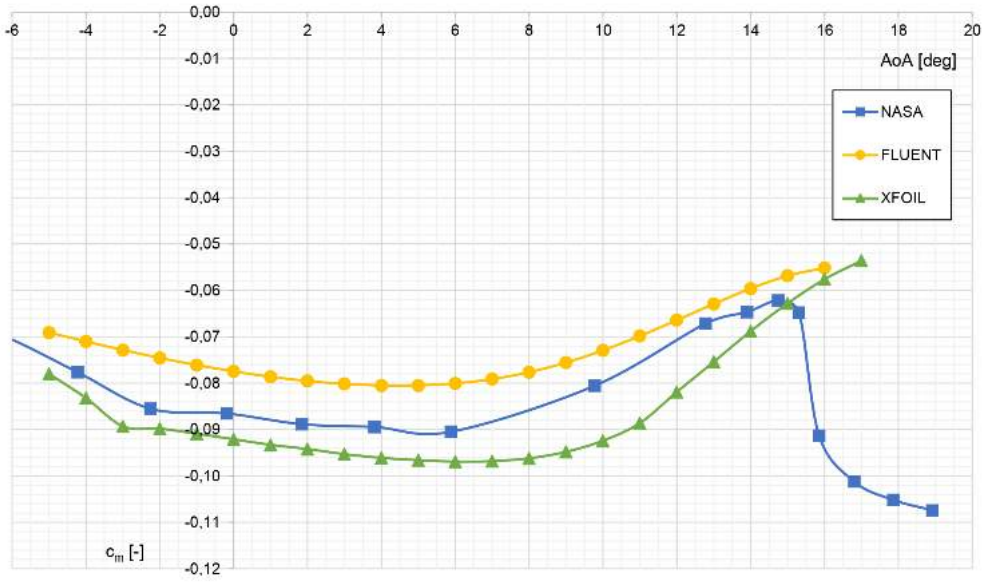

Fig. 4.4: Validation: moment curve.

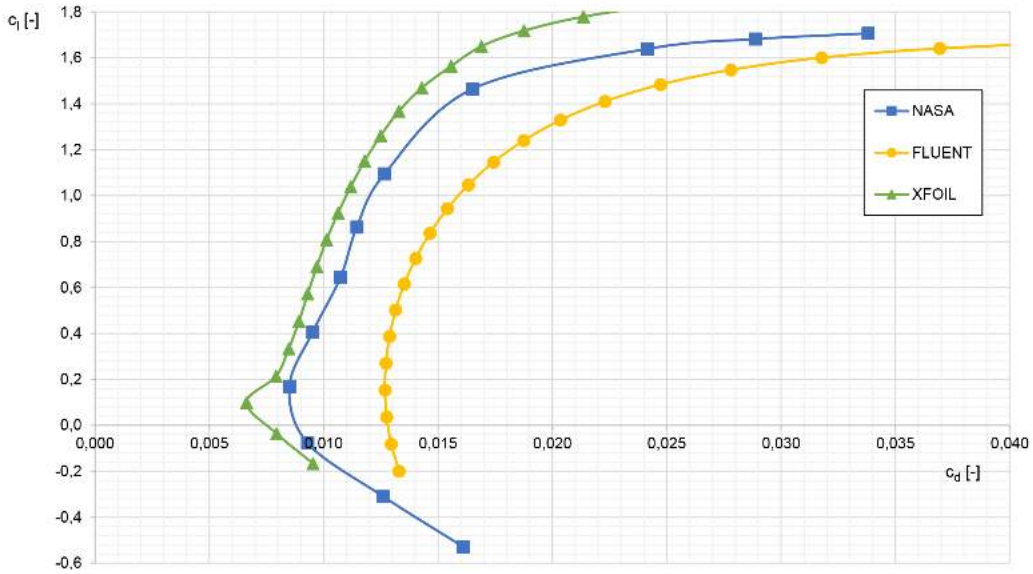

Fig. 4.5: Validation: polar curve.

The match with the experimental results on lift curve is significant. All values are copying the shape of the curve with the maximum deviation on maximum lift coefficient less than **3%**. Also, the point of maximum lift coefficient was predicted with sufficient accuracy within 1 deg of AoA. In the terms of the moment curve

the accuracy is significantly lower. The maximum deviation lies at -2deg and 6deg of AoA with its value of **13%**. Also, on the simulated moment curve the inflection point on higher AoA is over-predicted. From three monitored characteristics drag polar curve is the one least representing the experimental data. Maximum deviation is around **30%** which reflects poor quality. This is, unfortunately, very common for such type of solver. The error is mostly related to BL treatment and can be overcome only by transient, high-performance methods which are not cost and time-effective for studied case [23].

The best way to simulate such a flow is, in the term of cost-effectiveness, the panel method which is here represented by the XFOIL data. However, the accuracy is limited to the little range of AoA which is related to low occurrence of vortices and eddies.

The validation process proves the model applicability on selected task. Errors and deviations were taken into account when evaluating further simulation results. Numerical results of simulated and experimental data can be found in Appendix A.

5 NUMERICAL STUDY OF FLAPPED AIRFOIL

By establishing computational method the 2-dimensional investigation on airfoil equipped with rigid flaps can be performed.

5.1 Objectives

The purpose of this study is to properly simulate flow over the airfoil equipped with movable flaps. The goal is to find optimal flap properties such as length, deflection and position on the airfoil to generate significant increase of the performance of the airfoil. The optimization process is mainly driven by the lift curve and connected maximum lift coefficient location. In numerical flow simulation, flap is considered to be ridig. This allows the author to obtain the pressure distribution on the flap. This load distribution is then transferred to the structural analysis which determines the flap bending stiffness required for the flap automatic work.

5.2 Simulation Set-up

This section describes the overall progress of numerical set-up and analysis.

5.2.1 Geometry

In order to equip the airfoil with movable flap parametric model was utilized. The important parameters are marked in the figure 5.1.

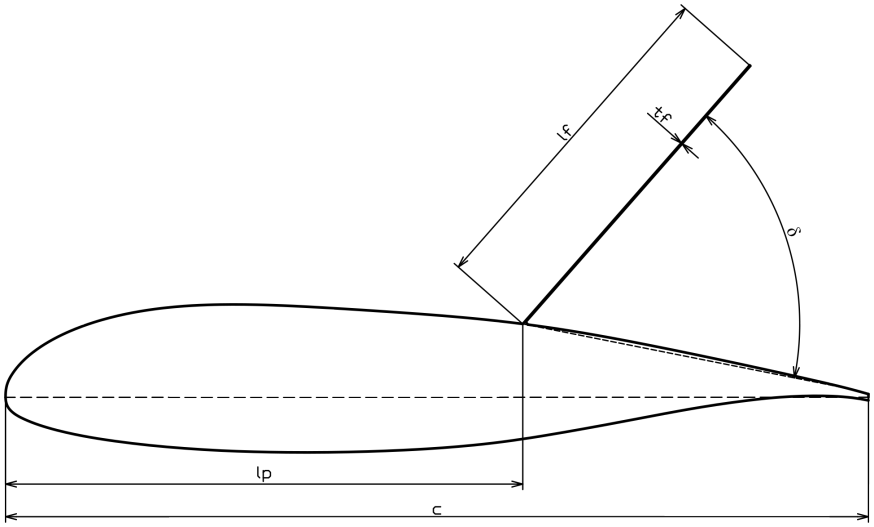

Fig. 5.1: Geometry of the flapped airfoil.

The parameter l_f marks the flap length, l_p denotes the position of the flap, the t_f is the flap thickness and δ represents the deflection angle.

5.2.2 Cases Assessment

Coded naming of single cases was introduced to account multiple parameters as:

$$F\_ww\_xx\_yy\_zz$$

where ww is a number denoting the flap position on the upper curve, xx is a number representing the flap length, yy is a number for deflection of the flap (related to the airfoil shape) and finally the zz which is representing the angle of attack of studied case. Flap thickness is determined as a constant value since it has little impact to observed phenomena. All numbers, except the deflection of flap which is given in degrees, are given in percentage of the chord of the airfoil.

The studied cases were chosen in respect to the findings of other authors presented in the chapter 2.1. List of studied cases is presented in the table 5.1 below:

Case	Position [%]	Length [%]	Deflection [deg]
F_80_20_20_zz	80	20	20
F_80_20_40_zz			40
F_80_20_60_zz			60
F_70_30_20_zz	70	30	20
F_70_30_40_zz			40
F_70_30_60_zz			60
F_60_40_20_zz	60	40	20
F_60_40_40_zz			40
F_60_40_60_zz			60

Tab. 5.1: Parameters of studied cases.

Number of cases was reduced by neglecting the cases with short flaps on different positions on airfoil. This was done in accordance with the statement in the chapter 2.1.3 which proves ineffectiveness of short flaps. Also, regarding the claim published by Brechert in the chapter 2.1.1 the flap actual length is always 1% (of the airfoil chord) lower than marked. This makes the 20% long flap to be 19%, 20% flap to be 19% long flap etc. The deflection angle was chosen to address both the influence of low-deflected and high-deflected case.

5.2.3 Computational Grid

The modified geometry was the main reason for choosing hybrid type of mesh. On lower angles of deflection of the flap the small angle between the flap and the airfoil was causing appearance of very skew quads. This led the author to use of triangular elements in the 'pocket' as shown in the picture 5.2. Motivation for this is the anticipated occurrence of low-speed vortex past the flap. Hence, the the energy of the flow is too low to form any sort of boundary layer in the near wall region. This presumption is proved by visual analysis of the flow presented in the figure 5.3. It is clearly seen that the order of velocity magnitude in recirculation region is much lower. The rest of the domain was meshed with the parameters set by mesh independence study.

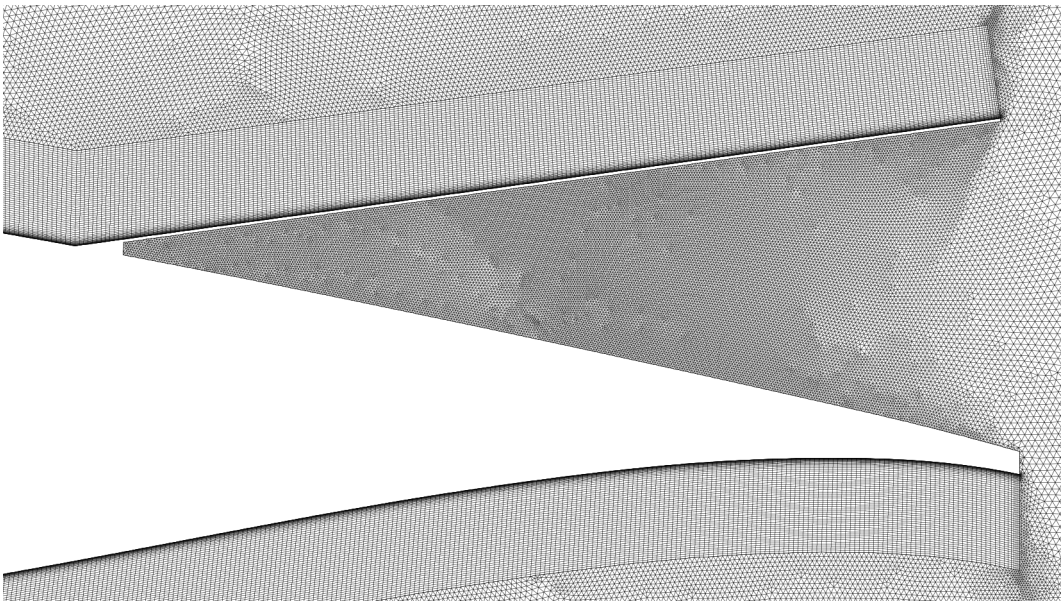

Fig. 5.2: Detail of mesh generation in the aft part of the airfoil.

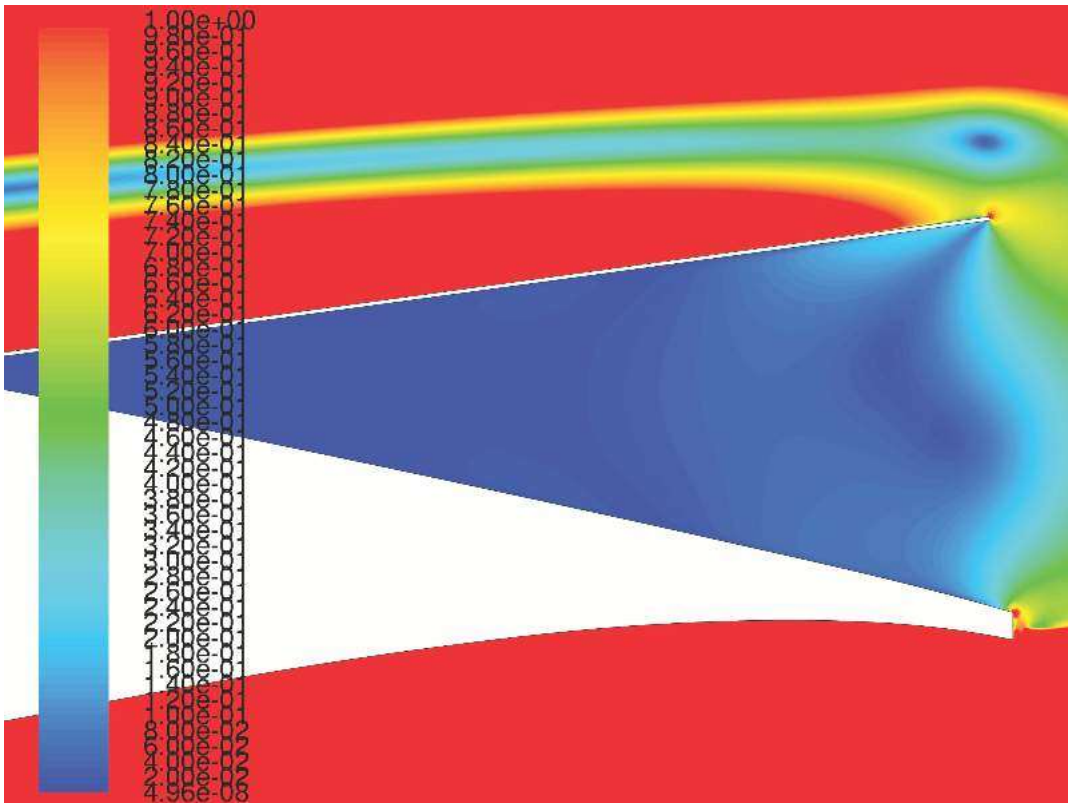

Fig. 5.3: Velocity magnitude in pocket region (Contour range is limited for better visualization).

5.2.4 Transient Simulation Set-up

Solver Settings

Since the unsteady behaviour like vortex shedding, strong turbulence formation is expected on higher angles of attack solution method that can handle such unstable flow must be employed. For the optimization purposes the unsteady RANS (**URANS**) method is introduced. While the other transient methods (SAS, DDES, LES, etc.) are much more precise, their computational requirements such a mesh resolution, computer memory and computational time are usually way bigger. This led the author to use same method presented in the chapter 3.3.2 which is the SST k-ω model but with transient option enabled. By the nature of the solver, standard URANS does not provide valid information of the turbulence spectrum. URANS models are working in a single mode vortex shedding which results in a vortex stream extending far behind the wake. This behaviour is related to the URANS inability to model wider range of length scales which appear in such a turbulence flow. Also, the URANS models tend to overestimate pressure in close proximity of the body.

This must be taken into account when evaluating the results [24] [25].

The transient simulation was set up with following parameters in the table 5.2:

Pressure - Velocity Coupling	
Scheme	Fractional Step
Spatial Discretization	
Gradient	Least Squares Cell Based
Pressure	Second Order
Momentum	Second Order Upwind
TKE	Second Order Upwind
Specific Dissipation Rate	Second Order Upwind
Transient Formulation	Bounded Second Order Implicit

Tab. 5.2: Transient simulation settings.

The settings of spatial discretization correspond to the one described in the chapter 3.3.2. Transient formulation is chosen as **Non-Iterative Time Advancement**. This method is using no outer iterations which significantly reduces the computing time. According to the reference [20] this scheme is denoted to be the fastest by the means of convergence. By enabling the NITA scheme the pressure-velocity coupling method **Fractional Step** can be picked. This method is less computationally expensive compare to other choices. To achieve better numerical accuracy after a series of time-steps the transient formulation is changed from first order to bounded second order. The advantage over a standard second order formulation lies in improved stability of solution [20] [19].

Time Discretization

In transient simulations the variable called time-step plays major role in solutions accuracy and stability. Wrong choice of this variable can lead to solution divergence or non-physical results. In order to successfully simulate turbulent structures the general condition is raised as [19]:

$$CFL \approx 1\,[-] \tag{5.1}$$

This recommendation cannot be applied on the whole domain due to the appearance of tiny cells near wall. Therefore, the application is limited to the region

of larger vortices in the wake. The value of time-step can be now estimated by employing the formula [19]:

$$\Delta t = \frac{CFL \cdot \Delta x}{U_\infty} \, [s] \tag{5.2}$$

Where Δt denotes the time-step size and Δx represents the mesh element size. Substituting the element size by the maximum cell size in refinement area around the airfoil (0.005m) the first guess on the time-step is equal to:

$$\Delta t = 0.0003 \, [s]$$

In order to save computation time the idea is to have the time-step as big as possible. Due to this fact, time-step independence study is carried out. The results are shown in following figures 5.4. Single values can be found in the table 5.3.

Δt [s]	0.01	0.001	0.0001	0.00001
c_l [-]	1.030	1.066	1.063	1.065
c_d [-]	0.036	0.056	0.063	0.063
c_m [-]	-0.015	-0.023	-0.022	-0.023
Difference				
Δc_l [%]	N/A	3.5	0.3	0.3
Δc_d [%]	N/A	56.0	12.8	0.7
Δc_m [%]	N/A	52.7	4.4	5.3

Tab. 5.3: Time-step independence study.

From the results is clearly seen that the case for the Δt of 0.0001 is sufficiently independent. This value lies close to the predicted value in equation 5.2. One has to also note that this was the biggest value of time-step where the second order transient formulation could be applied. The time-step size also determines the spectrum of turbulence modelled which is directly affecting the pressure drag in the wake. The structure of before-mentioned cases are presented in the Appendix figure A.1.

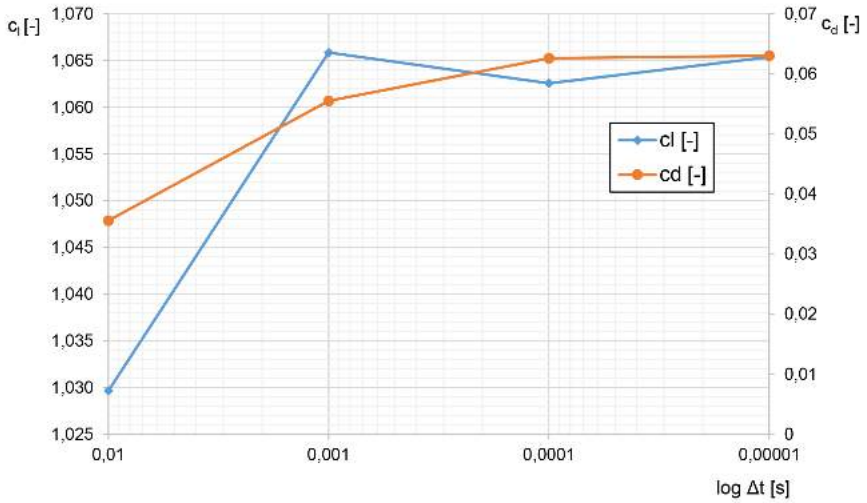

(a) Lift and drag coefficient vs. time-step size.

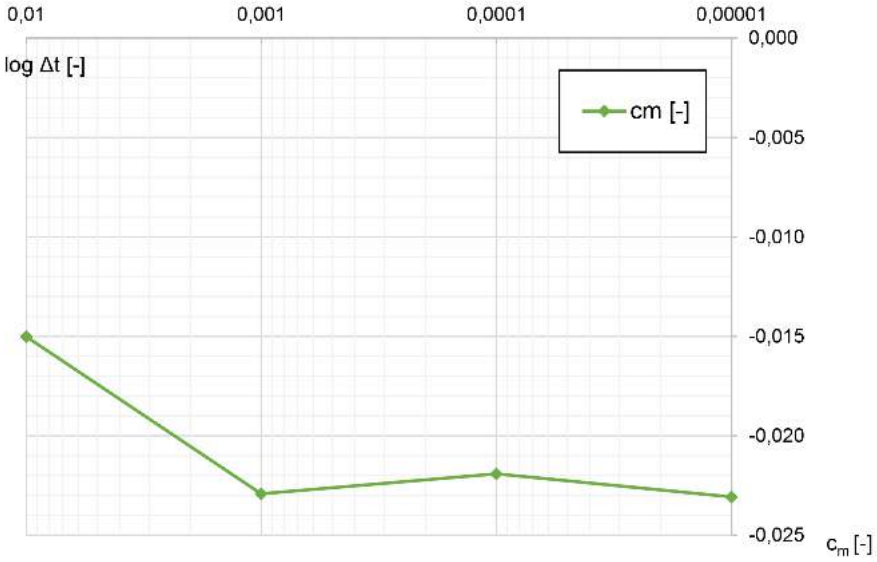

(b) Moment coefficient vs. time-step size.

Fig. 5.4: Monitored variables of time-step independence independence study.

Convergence

Convergence of monitors was evaluated in separated file. Due to the transient set-up also the monitors reported unsteady behaviour. In this case, the solution was proclaimed as converged as soon as the monitors showed levelled repetitive pattern in time history. An example of converged solution is presented in the picture 5.5.

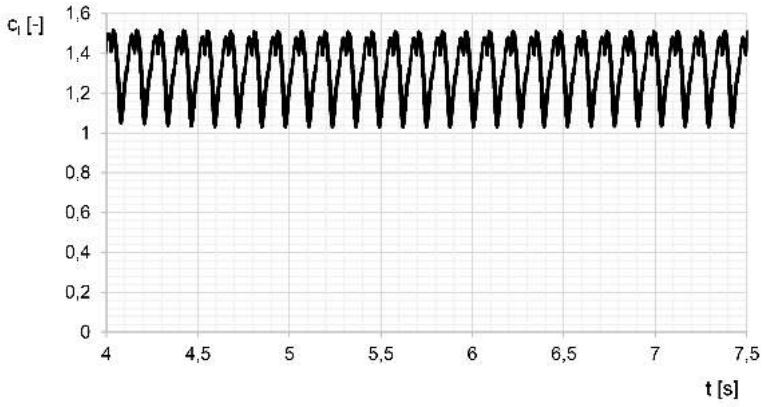

Fig. 5.5: Converged solution.

The desired value was obtained as an average over time-step:

$$c_l = \frac{1}{T - t_0} \int_{t_0}^{T} c_l(t) dt \, [-] \tag{5.3}$$

Where t_0 indicates the initial flow-time of time-averaging and T represent the final time-averaging flow-time. The flow-through time is establish as [24]:

$$T_{ft} = \frac{2d}{U_\infty} = \frac{2 \cdot 50}{14.607} = 6.8 \, [s] \tag{5.4}$$

Where d denotes the radius diameter. Usually, it took 1-2 flow-through times to get converged solution. On higher angles of attack, the converged solution required 3-4 T_{ft}. Together with the chosen low time-step the flow-through time indicates high computational-time requirements.

6 CASE RESULTS

In this section the results for various cases are presented together with the final comparison. The goal on each case was to find maximum lift coefficient corresponding to actual flap deflection. The flap thickness remains constant with its value of 1% of chord. The rough step of 4deg between each AoA was chosen in order to minimize computational time. Only in the last series of cases with the longest flap the step was decreased to 2deg to obtain more accurate results.

6.1 Flow Analysis

Behaviour of the flow can be split into three typical phases which determine the overall performance of the airfoil. The process of flow separation on high angles of attack is visualized by the means of contours of mean X-velocity presented in appendix B.

6.1.1 1^{st} Phase

First regime is characteristic with deflected flap protruding into the mean flow. This spoiler-like behaviour is also reflected in the lift and drag coefficient. The lift curve is shifted to the right which is indicating the decrease of airfoil performance. In this phase, also drag coefficient is rising. This deleterious phase is undesirable and should be avoided. In the case of self-adapting flaps the flap should be pushed downward due to the increased pressure on the upper side of the flap. This regime is demonstrated in following figure 6.1:

6.1.2 2^{nd} Phase

By next increasing of the angle of attack, the flap is preventing the recirculation area from further spreading. This behaviour has feasible impact on the aerodynamic characteristics. The lift coefficient is in this case reaching its maximum values. On the other hand, drag coefficient tends to decrease. This is given by the non-disturbed flow streamlines which are passing the flap in convenient manner. This is visualized in the figure 6.2. This act agrees with the measured and modelled cases of other authors who claimed that the best performance of the flap was spotted when the flap was slightly touching separated shear layer [4].

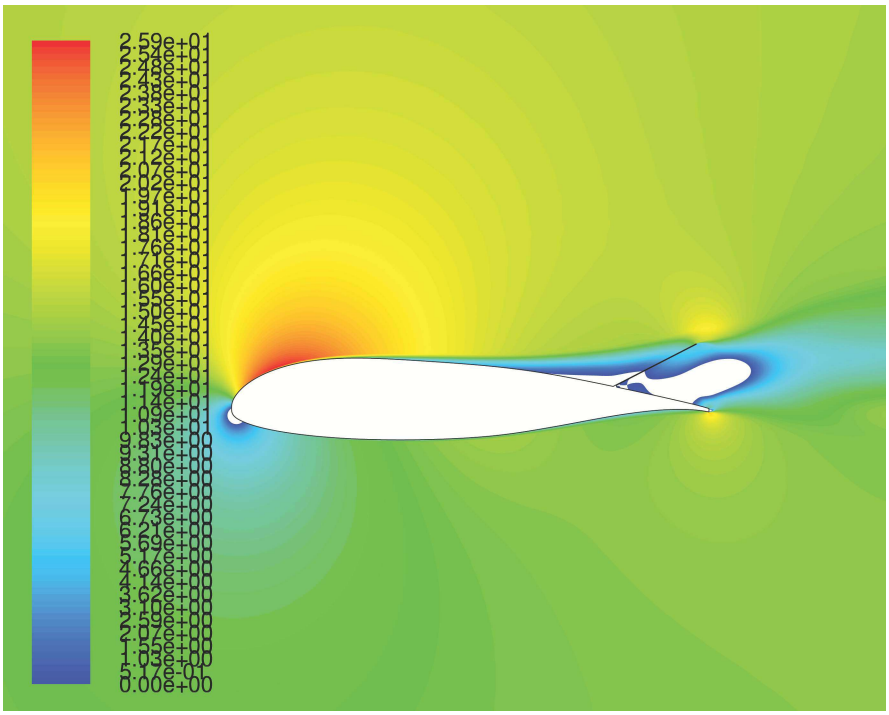

Fig. 6.1: Phase 1: Contours of mean X-velocity with the minimum value 0.0 in the case F_80_20_40_14. Spoiler-like behaviour of the flap.

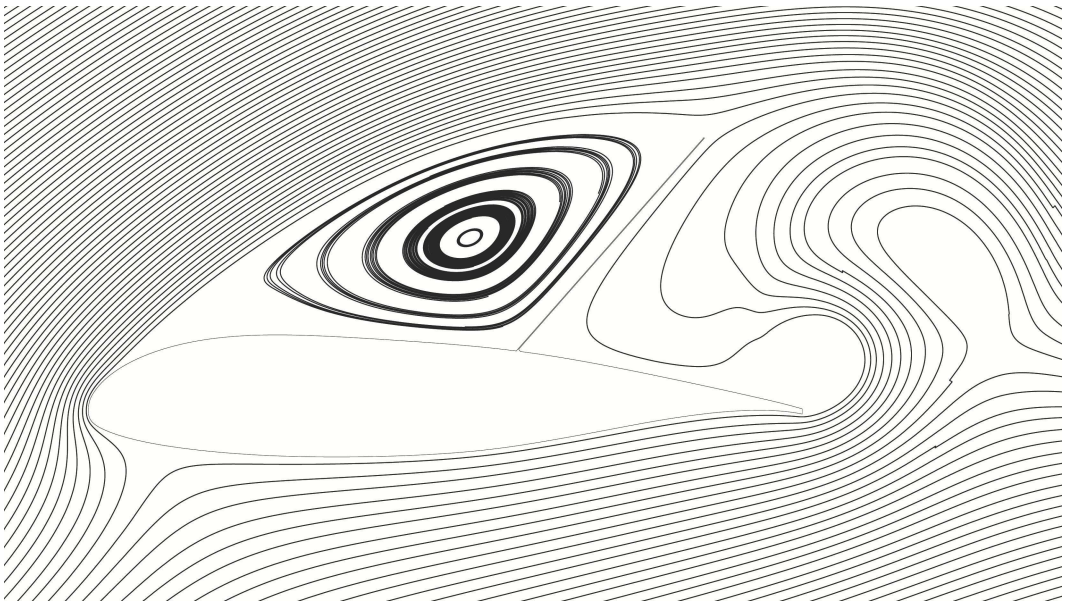

Fig. 6.2: Phase 2: Pathlines in the case F_60_40_60_26.

Also, the drag reduction is also related to the leading edge vortex shedding which is much more stabilized by the presence of the flap [6]. In the lift to drag ratio curve

this phase is indicated by little bump in the curve which can be observed on all cases in the appendix C. The strong lift coefficient increment is also related to the enhanced moment coefficient magnitude which is also reaching higher values.

As can be observed in the figures 6.2 and 6.3 the swirl is generated in the valley located upstream, near the intersection of the flap and the airfoil. The vortex is also creating local low-pressure region which greatly improves the lift coefficient. This behaviour is very similar to the corrugated surface case presented in reference [1]. This rough surface with little valleys allows creating of small vortices which are trapped inside. Although the authors cannot agreed on the principle behind this phenomena the resulting lift increment is promising more future application.

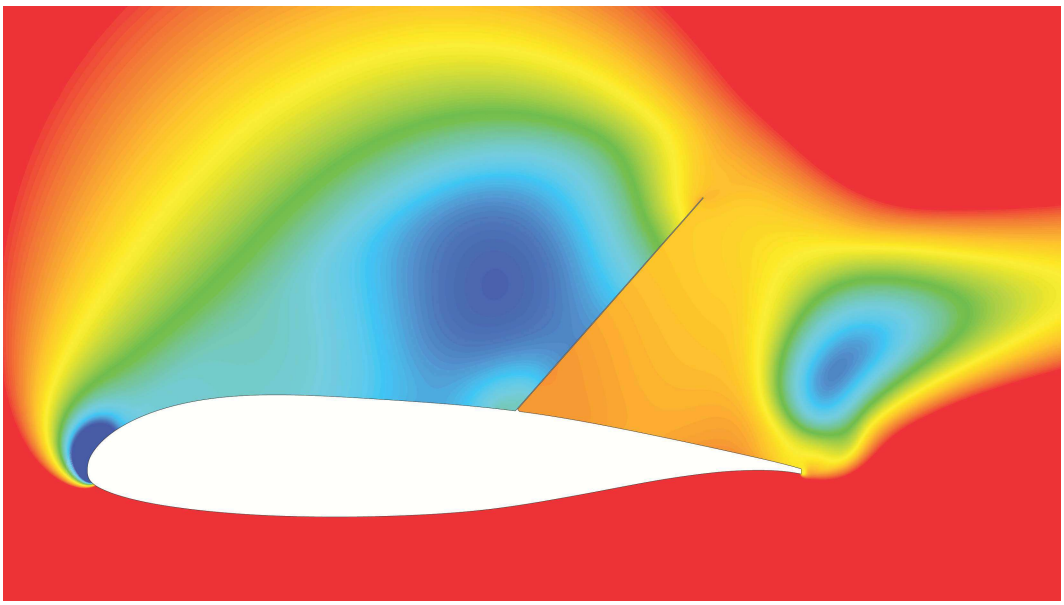

Fig. 6.3: Clipped pressure distribution around the airfoil. Case F_60_40_60_26. Blue represents the area of decreased pressure whereas red indicates higher pressure areas.

The increased pressure in the pocket, as observed in the figure 6.3, is forcing the flap to be raised from its natural position. This implies the use of self-adjusting flaps which according to distributed pressure along the flap length can set itself to the appropriate position.

6.1.3 3^{rd} Phase

Further increment of the angle of attack results in decrease in the aerodynamic performance. The magnitude of pressure and connected velocity decreases behind the leading edge of the airfoil. The vortex region behind the flap grew in such a size

that the flap can no longer prevent the recirculation region from spreading upstream. The process is related to the overall degradation of aerodynamic characteristics: lift coefficient decreases, moment coefficient also decreases and the drag is rising. Such a case in demonstrated in the figure 6.4.

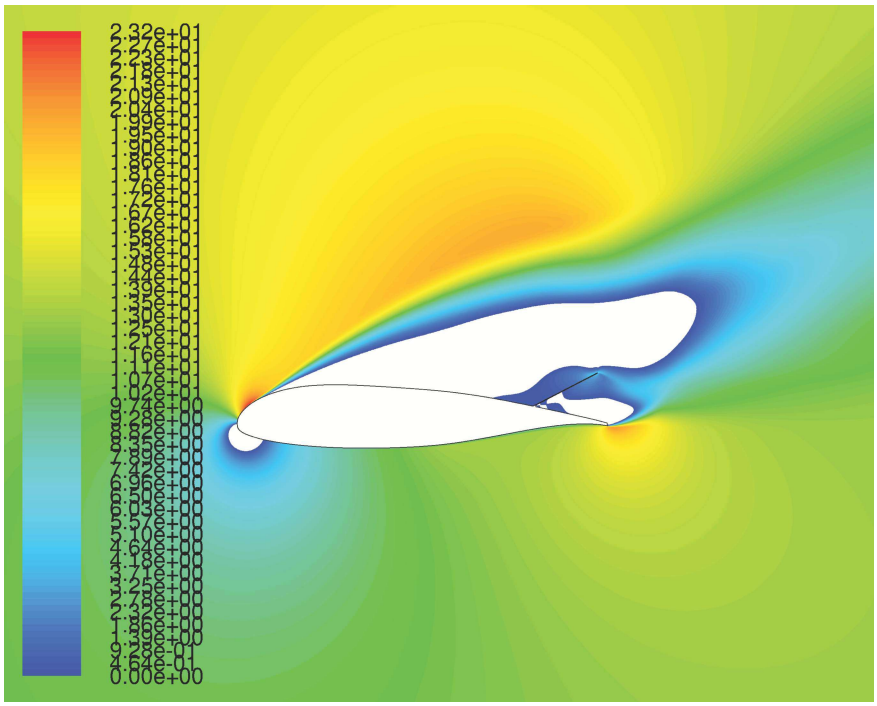

Fig. 6.4: Contours of mean X-velocity with the minimum value 0.0 in the case F_80_20_40_26. Decrease of aerodynamic characteristics.

In this figure 6.4 the recirculation region has passed the flap and massively increased its size. This behaviour is typical for the situation of stall of the clean wing (clean airfoil).

6.2 Results Comparison

The study began with the shortest flap located furthermost on the airfoil. To keep the paper well-arranged only the lift curve is presented below. Moment curve, lift to drag ratio together with the tabular data are shown in the Appendix C.

6.2.1 20% Flap Cases

The sections of the lift curve for the shortest flap are shown in the figure 6.5:

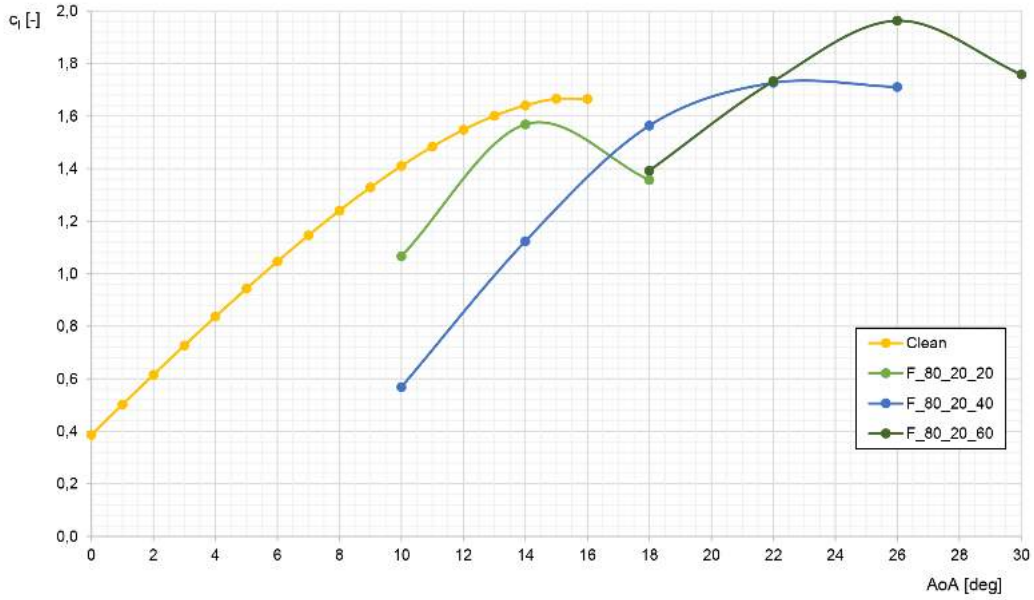

Fig. 6.5: Lift curves of the F_80_20 cases.

At first glimpse it is clear that the most effective flap is the most deflected in the terms of maximum lift coefficient. In the most deflected case the maximum lift coefficient yields the value of **1.96** which is significant increase to the clean airfoil configuration (max. value of 1.67) whereas the low deflected case shows decrease of the maximum lift coefficient. The critical angle of attack is shifted towards the higher values on the more deflected cases. The moment curve presented in the figure C.2 shows massive increase of the moment coefficient which is clearly related to the increase in the lift force. Drag to lift ratio curve as presented in the figure C.1 proves the overall decrement of the ratio.

6.2.2 30% Flap Cases

The next series of cases were focues on longer flap located further upstream. From the graphs it can be seen that the longer flap produces higher lift increment. The case with low-deflected flap is again not very effective. This can be addressed to the low deflection of the flap and inability of holding up the spreading vortex. Expectably, this case has the best lift to drag ratio from all three cases. The F_70_30_40 case shows drastic improvement in the terms of lift. Lift curve of this case is shifted more to the right than the previous case of shorter flap. As in the first case, best performance shows the most deflected case. The maximum lift coefficient obtained from simulations is **2.06**.

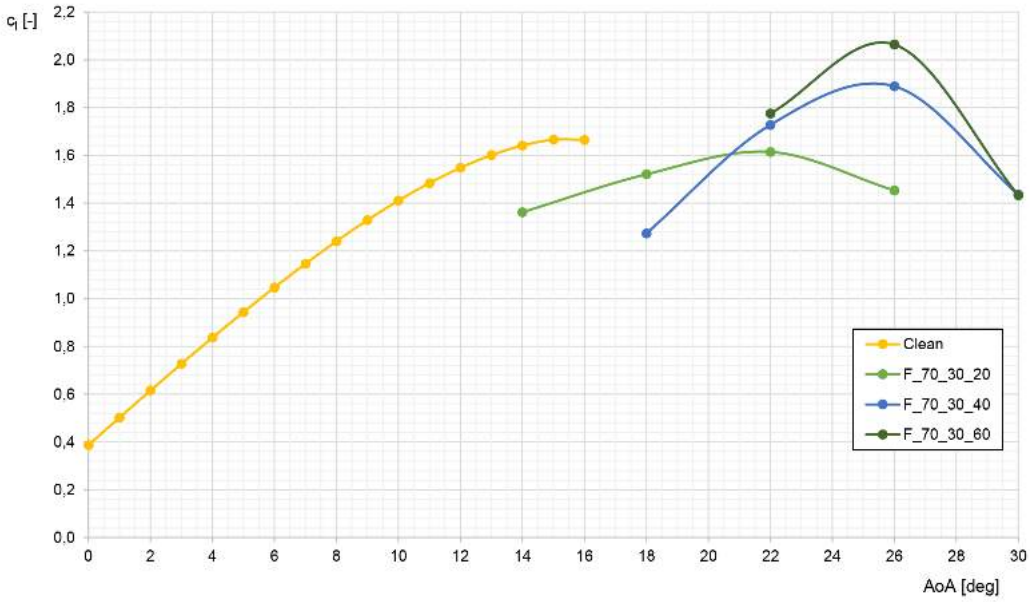

Fig. 6.6: Lift curves of the F_70_30 cases.

6.2.3 40% Flap Cases

based on the facts noted in the chapter 2.1.2 the last studied series of cases with longest flap promised superior performance. As in the first to cases, the low-deflected flap shows weak performance. The only difference to the previous results is maximum lift coefficient on two angles of attack separated by low value of c_l. The quick look on the velocity contours proves the flap functionality on 18deg of AoA. On higher angles of attack the flow is completely separated. This is also visible on the lift to drag ratio curve where the maximum is also located on the 18deg of AoA. The behaviour on angles past the critical angle of attack is also very interesting for

further study. Unfortunately, the method used for the purposes of presented study is not well suited for such a application.

The more deflected case shows again drastic improvement in the lift coefficient. The curve is no longer shifting to the right, the AoA related to the maximum lift coefficient stays the same. The greatest maximum lift coefficient was obtained in the most deflected case of 40% long flap. The value **2.41** was achieved on 28deg AoA. Expectably, the maximum lift coefficient also yields maximum moment coefficient.

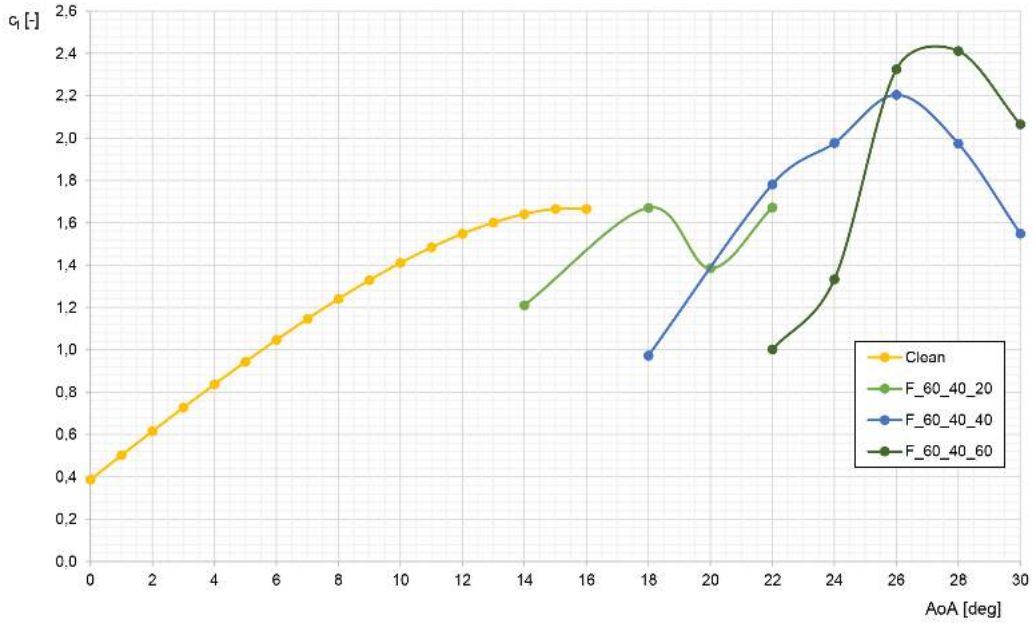

Fig. 6.7: Lift curves of the F_60_40 cases.

6.3 Discussion

The before-presented results prove the initial guess. The longest studied flap operating at its biggest deflection also achieved biggest lift coefficient increment. This finding agrees with the experimental results presented in [3]. The comparison between each case in terms of maximum lift is presented below in table 6.1. The percentage difference is presented relatively to the maximum lift coefficient obtained from the validation of the clean airfoil:

Maximum lift coefficient c_{l_max}			
δ [deg]	20% Flap	30% Flap	40% Flap
20	1.57	1.61	1.67
40	1.73	1.89	2.20
60	1.96	2.06	2.41
Difference			
$\Delta c_{l\_max\_20}$ [%]	-5.8	-3.1	-0.4
$\Delta c_{l\_max\_40}$ [%]	3.7	13.4	32.3
$\Delta c_{l\_max\_60}$ [%]	17.9	23.9	44.8

Tab. 6.1: Maximum lift coefficient comparison.

This table shows superior performance of high deflected flaps ranging from **18% to 45%** gain to the clean airfoil. In contrary, the low-deflected flaps show minor decrement in lift coefficient. In all cases the critical angle of attack was strongly increased reaching the value of **28deg** in the F_60_40_60 case. Since the step between each AoA was too large to accurately predict the critical AoA the comparison of various critical angles of attack is not present.

In the terms of drag with increasing lift, the drag is also rising rapidly. This is due to the massive wake which is created on higher angles of attack and connected increment in pressure drag. Since the moment coefficient is strictly related to the lift coefficient the rapid increase in moment magnitude was expected. The values on critical angles of attack are reaching the magnitude of **0.58**.

6.4 Solution Evaluation & Accuracy

As mentioned before, the results must be very carefully evaluated. Due to URANS inability to model wider range of turbulence it often results in over-prediction in pressure. Therefore, it is possible for better numerical method or wind-tunnel experiments to measure less pressure in the proximity of airfoil causing a decrement in lift and drag force. In order to get more valid results the 3-dimensional domain with a segment of flap and wing should be utilized together with more advanced method such as LES or DES which allows to resolve and model wider spectrum of turbulence.

The major issue arised during the simulation was the computational time. Usually, the convergence time and rate was good in situations related to 1^{st} phase (low angles of attack) with low deflections of the flap. The problems arises on higher

angles of attack. The convergence rate rapidly decreases after implementing second order of transient formulation. Also the instability of residuals often forced the author to go for smaller value of under-relaxation factors which also slowed down the convergence. In conclusion, it usually took 1-2 flow-through times to converge on Phase 1 and 2 cases which equals up to 26 hours on 24-core cluster. The computational time was higher on Phase 3 cases which usually took around 2-4 flow-through times to converge. These simulations reached up to 53 hours of computation on 24-core cluster.

Even though, the computational time was higher still the URANS method was the one most applicable for the purposes of optimization of the airfoil equipped with flap. By using this method one is able to get somewhat valid idea of the flow behaviour and its effect on the aerodynamic characteristics.

7 STRUCTURAL ANALYSIS

In order to acquire load distribution on flap in a simple manner the flap was modelled as a straight and rigid. The idea behind self-adaptive movable flap is that it can set itself to desired position. By the means of flap bending stiffness the deflection angle can be adjusted to the desired optimal position. The case generating maximum lift coefficient (F_60_40_60_28) was chosen as a design point for flap bending stiffness.

7.1 Load Distribution

The post-proccessing of the results from case F_60_40_60_28 was done. Through the calculation, *Data Sampling for Time Statistics* was enabled allowing the software to time-average desired variables. The total pressure is defined by Fluent as [19]:

$$p_0 = p_s + p_d\,[Pa] \tag{7.1}$$

Where the p_0 denotes the toal pressure, p_s marks the static pressure and p_d determines the dynamic pressure. From theory, the dynamic pressure on the wall should be zero since the condition assigned to the wall is no-slip (with zero velocity on this BC). This yields that the only acting pressure on the surface is the static pressure. So, the next step is plotting the pressure distribution along the boundary of the flap. The resulting load on the upper and lower side is presented in the figure 7.1. The pressure distribution was sampled on 200 points.

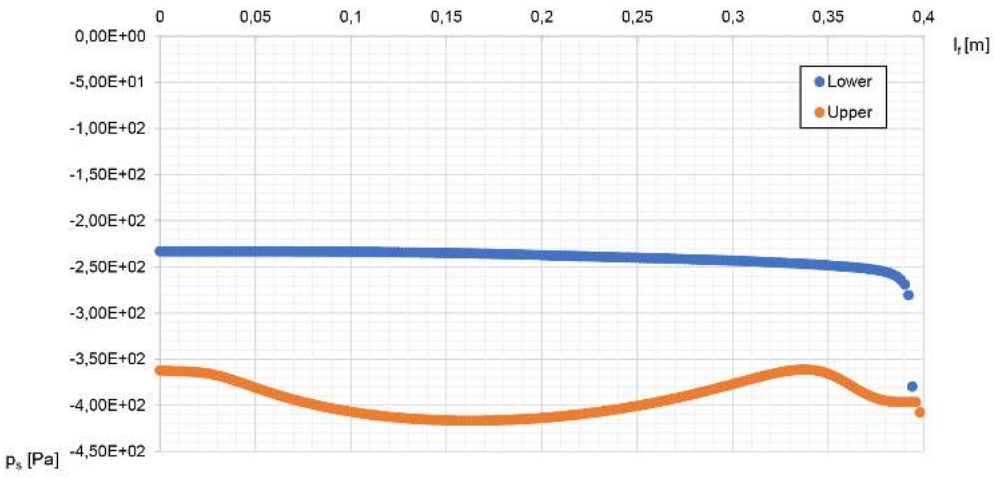

Fig. 7.1: Pressure distribution on the flap. Case F_60_40_60_28.

From the graph 7.1 is clearly seen the lower pressure acting on the upper side of the flap. This is also clear from the figure 6.3 which is showing the pressure distribution in the flow field. The final load acting on the flap is generated by subtraction values of upper and lower side.

7.2 Computational Model

The elastic flap is deflected by the operating pressure which causes big displacement of the tip of the flap. This is demonstrated on the following picture 7.2:

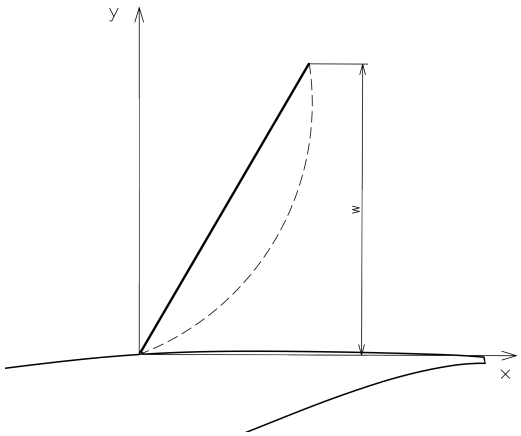

Fig. 7.2: Elastic flap parameters. Dashed line symbolized predicted deformed shape.

Where the w is the maximum displacement of the flap. Desired displacement as measured in Catia software yields the value of :

$$w_{mod} = 0.344\,[m]$$

As can be seen the expected displacement is going to be high. This fact excludes the linear beam theory and connected analytical solution. Although there were developed closed-form method for establishing large displacements in these days the user-friendly FEM software simulation is in many ways more convenient way [26].

7.3 Finite Element Method

In order to simulate such a non-linear case the ANSYS structural package was utilized. This professional software is used in many engineering application often with great success. Despite this, some sort of validation must be done.

7.3.1 Validation

Since presented case is going to be modelled as 3D beam relevant validation case was sought. The experimental and numerical study on cantilever beam presented in the reference [27] was chosen. Here, simple cantilever beam is loaded by by external concentrated load as shown in the following figure 7.3:

Fig. 7.3: Experimental set-up [27].

The paper presented measured data for various loading. Regarding studied case only the displacement caused by greatest force was considered. Considering this condition the maseaured displacement at the end of the beam is [27]:

$$w_{val\_exp} = 0.281\,[m]$$

The geometry of the experimental case was recreated using the ANSYS Modeler using the simple line body with assigned cross-section. The material was assigned so that the value of Elastic modulus is in accordance with the experiment data. The line-body was meshed with 200 elements to account further research on elastic flap. The load and fixed boundary condition was implemented to accurately represent the experiment. Additionally, the analysis was set up to iterative non-linear regime to properly simulate larger displacements. The resulting simulated displacement is shown in the picture 7.4.

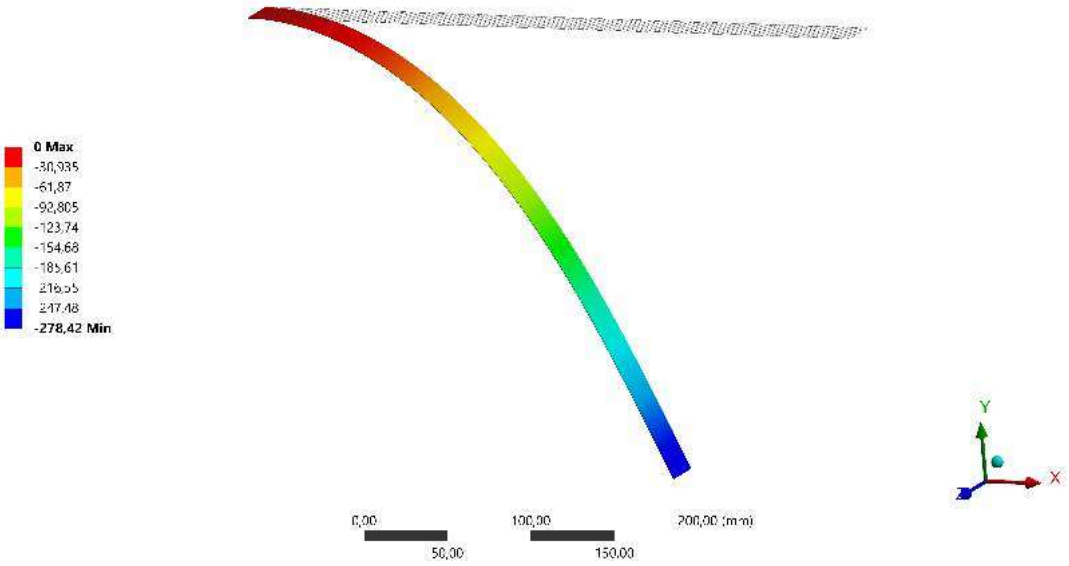

Fig. 7.4: Displacement plot of validation case in Ansys mechanical.

The maximum deflection from the simulation was obtain as a:

$$w_{val\_num} = 0.278\,[m]$$

It is obvious that the results agreed very well. The relative error is about 1% which indicate well validated case.

7.3.2 Structural Analysis of Elastic Flap

The structural analysis of elastic flap was performed in respect to the findings made in previous chapter. The flap was modelled as a 3-dimensional beam with constant quadrilateral cross-section which reflected the flap thickness. The beam was split to 200 bar elements to account the number of single loads together creating distributed load. The loading resulting from the flap mass was due to its low value neglected. Then, according to the results made in the chapter 7.1 list of loads was imported to the FEM software. The meshed beam is shown in the appendix, in the figure D.1.

Series of simulations was run with variable of Elastic modulus to obtain optimal displacement noted beforehand. After several iterations, the optimal Elastic modulus E was found together with the moment of inertia I. The deformed shape is shown in the figure 7.5 below:

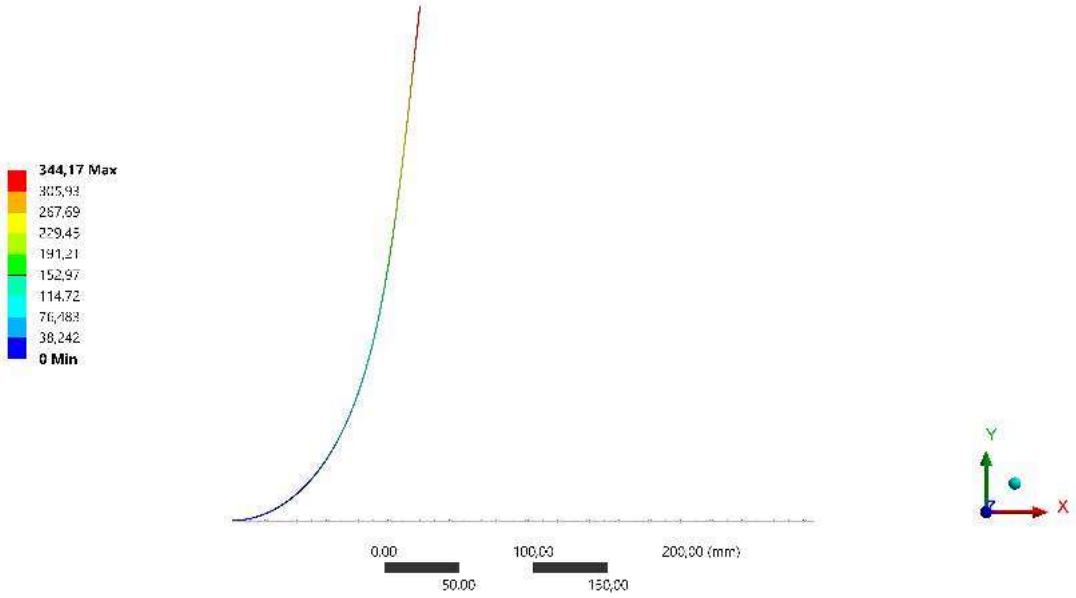

Fig. 7.5: Displacement plot of case study in Ansys mechanical.

The value of maximum displacement is:

$$w = 0.344\,[m]$$

The maximum value of bending stress was calculated as:

$$\sigma_o = 32.1\,[MPa]$$

The product of moment of inertia and elastic modulus create a variable called **flexural rigidity** or bending stiffness. In the case of elastic flap this value was computed as [27]:

$$EI = 2.685e^{-4}\,\left[Nm^2\right]$$

8 FINAL ASSESMENT

In this chapter the flow-field and aerodynamic performance changes, which arised due to the deformed shape of the flap, are investigated. The coordinates of the center-line were extracted from the Ansys Mechanical and imported to the graphical software. The domain was re-meshed accordingly and the simulation was set in accordance with the set up in F_60_40_60_28 case. The differencess are presented in the table 8.1:

F_60_40_60_28 Case		
	Rigid Flap	Elastic Flap
c_l [-]	2.41	2.267
c_d [-]	0.642	0.615
c_m [-]	-0.575	-0.512
Difference		
Δc_l [%]	6.0	
Δc_d [%]	4.2	
Δc_m [%]	11.0	

Tab. 8.1: Comparison of aerodynamic characteristics between rigid and elastic flap.

As can be seen by introducing deformed shape of the flap the values of all monitored variables decreased. The comparison in the terms of X-velocity contours is presented below 8.1:

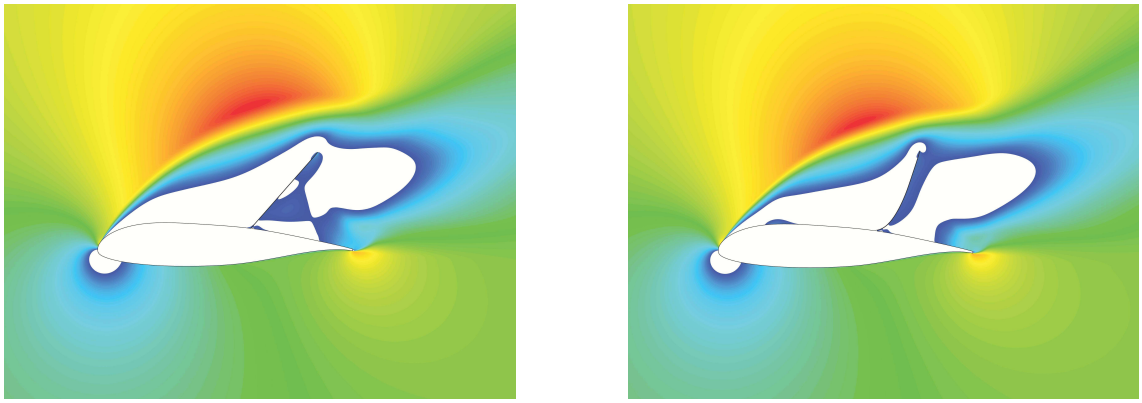

(a) Rigid flap.

(b) Elastic flap.

Fig. 8.1: Contours of mean X-velocity with the minimum value 0.0 in the case F_60_40_60_28.

The pressure distribution on the flap also caused slight shift of the flap tip to the left. From pictures above can be drawn that the flap is still in the phase 2. However, in the rigid flap case the recirculating region is slowly running over the tip of the flap causing the transition from the phase 2 to phase 3. This is not present in the case of elastic flap due to the reason stated in first sentence of this paragraph. Hence, the author presumes bigger lift coefficient on higher angle of attack. Due to time issues, this was not simulated but this analysis proved the concept of the elastic flap and its small influence of deformed shape to the aerodynamic characteristics.

9 CONCLUDING REMARKS

In this paper research on aerodynamic characteristics of airfoil equipped with flap is carried out. In the first chapters research history and the principle of movable flaps is explained. It is followed by overview of remarks made by other authors which was then used as a guideline for choosing characteristic cases. The paper continues with detailed discussion on numerical method choice. In addition, the geometry and mesh generation is briefly described. To verify the numerical method applicability the verification and validation process is utilized. Based on previous findings series of cases were set-up and resolved by using CFD software. In following chapter the flow-field analysis is done together with evaluation of results. Afterwards, the case producing highest lift force was used as an input to the structural analysis which determined elastic flap shape. Finally, this modified shape undertook CFD analysis and was compared to the previous performance of airfoil equipped with rigid flap.

The results presented above proves the concept of upper-surface flap. The similarity between the proposed 'Reverse flow bags' principle mentioned in the chapter 2.1 and numerical result is more than significant. As predicted, the longest flap achieved highest lift coefficient. The maximum lift coefficient was obtained for the case of elastic flap, 40% long, at 28deg of angles of attack as:

$$c_{l\_max} = 2.3\,[-]$$

The interesting question would be regarding the bigger flap deflection and bigger length. Remarks from wind tunnel tests implie that the bigger deflection on self-adaptive flaps is causing the flap to tip over in the forward direction [3]. That was main reason for the studied range of deflections in presented study. Also, using longer flaps than presented is questionable. Even though it promises higher lift coefficient increment the flaps rigidity must be also taken into account. The vortex which is being shed from the leading edge on high angles of attack is creating time-dependent oscillation in the flow field. This causes the variable load distribution on the flap and connected fluttering of the flap. This case does not have to be deleterious and can result into even better aerodynamic performance as presented in the reference [6].

Another interesting question would be about the number of used flaps. The reference [6] reported superior aerodynamic performance by using three successive flexible flaps. Since the number of cases rapidly rises when considering more flaps such a case was not discussed or studied in presented paper. Author implies of use similar computational method in order to evaluate the effect of multi-flap application.

Regarding the solution method used URANS method showed good performance. Despite its longer computation times for the optimization purposes this method

was appropriate choice. The use of velocity-inlet boundary condition as a flow inlet and outlet proved to be reasonable. The flow-field did not showed any non-physical behaviour and the solution was able to converge. This proved the velocity-inlet BC applicability in low-speed non-compressible cases. Since the turbulence phenomena shows 3-dimensional behaviour the author implies the use of segment of the wing equipped with flap for further analysis. The computational method should be on the level of scale resolving simulations such as LES or DES in order to properly capture the flow-field [12]. The top analysis would be the implementing of fluid-structure interaction. This module which is accessible for example in Ansys package allows to use coupled computation of both FEM and CFD. This high computational-cost method would enable to resolve the interaction between the flexible flap and air in time. By this process the flow behaviour could be described in detail and the flap further optimized in order to have practical usage.

BIBLIOGRAPHY

[1] CHOI, Haecheon - PARK, Hyungmin - SAGONG, Woong - LEE, Sang-im. *Biomimetic flow control based on morphological features of living creatures* [online]. [retrieved 20.10.2016] Available from: <www.researchgate.com>.

[2] *High-Lift Devices* [online]. [retrieved 26.11.2016] Available from: <www.aerospaceengineeringblog.com>.

[3] BECHERT, D.W. - HAGE, W. - MEYER, R. *Self-actuating flaps on bird and aircraft wings* [online]. Berlin, Germany: Department of Turbulence Research, German Aerospace Center (DLR), 2007. [retrieved 1.11.2016] Available from: <www.witpress.com>.

[4] MEYER, Robert - HAGE, Wolfram - BECHERT, Dietrich W. - SCHATZ, Markus - KNACKE, Thilo - THIELE, Frank. *Separation Control by Self-Activated Movable Flaps* [online]. AIAA Journal, Vol. 45, No. 1 (2007), pp. 191-199. [retrieved 10.11.2016] Available from: <www.dlr.de>.

[5] KERNSTINE, Kemp H. - MOORE, Courtney J. - CUTLER, Andrew - MITTAL, Rajat. *Initial Characterization of Self-Activated Movable Flaps,"Pop-Up Feathers"* [online]. Reno, NV: 46th Aerospace sciences meeting AIAA, 2008. [retrieved 10.11.2016] Available from: <www.engineering.jhu.edu>.

[6] BRÜCKER, Christoph - WEIDNER, Christoph. *Influence of self-adaptive hairy flaps on the stall delay of an airfoil in ramp-up motion* [online]. Freiberg, Germany: TU Bergakademie Freiberg, Institute of Mechanics and Fluid Dynamics, 2014. [retrieved 1.11.2016] Available from: <www.researchgate.com>.

[7] PATONE, Giannino - MÜLLER, Werner. *Aeroflexible Oberflächenklappen als "Rückstrombremsen"nach dem Vorbild der Deckfedern des Vogelflügels* [online]. [retrieved 26.11.2016] Available from: <www.bionik.tu-berlin.de>.

[8] SCHATZ, Markus - BUNGE, Ulf - LÜBCKE, Holger. *Numerical Study of Separation Control by Movable Flaps* [online]. [retrieved 26.11.2016] Available from: <www.cfd.tu-berlin.de>.

[9] McGHEE, Robert J. - BEASLEY, Wiliam D. *Low-Speed Aerodynamic Characteristics Of a 17-Percent-Thick Airfoil Section Designed For General Aviation Applications* [online]. NASA Langley Research Center, 1973. [retrieved 7.1.2017] Available from: <https://ntrs.nasa.gov>.

[10] McGHEE, Robert J. - BEASLEY, Wiliam D. - WHITCOMB, Richard T. *NASA Low - and Medium - Speed Airfoil Development* [online]. NASA Langley Research Center, 1979. [retrieved 7.1.2017] Available from: <https://ntrs.nasa.gov>.

[11] *UIUC Airfoil Data Site* [online]. University of Illinois at Urbana-Champaign, 2017. [retrieved 24.4.2017] Available from: <https://m-selig.ae.illinois.edu>.

[12] VERSTEEG, H. K. - MALALASEKERA, W. *An Introduction to Computational Fluid Dynamics: The Finite Volume Method*, 2nd edition, 2007. Harlow: Pearson Education.

[13] LOMBARD, Jean-Eloi. *Introduction to Structured Grid Generation for Aeronautics.* [online]. Lausanne: Swiss Institute of Technology, 2011. Semester project. [retrieved 1.4.2017] Available from: <http://www.lombardf.com>.

[14] CERMAK, J. - STAHLBOCK, L. *Diffusion, Convection-Diffusion and Numerical Diffusion.*. Linköping: Linköpings universitet, 2016. Semestr project.

[15] *Y plus wall distance estimation* [online]. 2011. [retrieved 28.4.2017] Available from: <https://www.cfd-online.com>.

[16] LANTZ, Jonas. *Computational Fluid Dynamics* Linköping: Linköpings universitet. 21 January 2016. Lecture

[17] McGHEE, Robert J. - BEASLEY, Wiliam D. *Wind-Tunnel Results for a Modified 17-Percent-Thick Low-Speed Airfoil Section* [online]. NASA Langley Research Center, 1981 . [retrieved 7.1.2017] Available from: <https://ntrs.nasa.gov>.

[18] BROŽ, Václav. *Aerodynamika nízkých rychlostí* Fourth edition. Praha: Vydavatelství ČVUT, 1977. ISBN 80-01-01367-7

[19] *ANSYS Fluent User's Guide* [online]. Release 15.0. U.S.A., 2013. [retrieved 1.5.2017] Available from: <http://www.ansys.com/>.

[20] *ANSYS Fluent Theory Guide* [online]. Release 15.0. U.S.A., 2013. [retrieved 1.5.2017] Available from: <http://www.ansys.com/>.

[21] *ANSYS ICEM Help Manual* [online]. Release 15.0. U.S.A., 2013. [retrieved 1.5.2017] Available from: <http://www.ansys.com/>.

[22] *Turbulence Part 4: Reviewing how well you have resolved the Boundary Layer* [online]. 2013. [retrieved 1.5.2017] Available from: <https://www.computationalfluiddynamics.com>.

[23] ELENI, Douvi C., - ATHANASIOS, Tsavalos I., - DIONISSIOS, Margaris P. *Evaluation of the turbulence models for the simulation of the flow over a National Advisory Committee for Aeronautics (NACA) 0012 airfoil* [online]. Patras: University of Patras, 2012. [retrieved 5.5.2017] Available from: <http://www.academicjournals.org>.

[24] MENTER, F. R. *Best Practice: Scale-Resolving Simulations in ANSYS CFD* [online]. ANSYS Germany GmbH, 2012. [retrieved 13.5.2017] Available from: <http://www.cfd.grs.de>.

[25] DEMETER, G. Fertis. *Nonlinear Structural Engineering: With Unique Theories and Methods to Solve Effectively Complex Nonlinear Problems* [online]. Germany: Springer-Verlag Berlin Heidelberg, 2006. [retrieved 13.5.2017] Available from: <https://www.springer.com>.

[26] YOUNG, M. E., - OOI, A. *Comparative Assessment of LES and URANS for Flow Over a Cylinder at a Reynolds Number of 3900* [online]. Australia: Department of Mechanical and Manufacturing Engineering University of Melbourne, 2007. [retrieved 13.5.2017] Available from: <http://citeseerx.ist.psu.edu>.

[27] BELÉNDEZ, T. - NEIPP, C. - BELÉNDEZ, A. *Numerical and Experimental Analysis of a Cantilever Beam: a Laboratory Project to Introduce Geometric Nonlinearity in Mechanics of Materials* [online]. Spain: Universidad de Alicante, 2003. [retrieved 17.5.2017] Available from: <https://www.ijee.ie/>.

LIST OF FIGURES

1.1 Leading edge slats as observed on the bird's wings [2]. 13
1.2 Slow approach by the Seagull with extended upper flaps. 14
2.1 Mechanism of the "Reverse Flow Bags"[7]. 15
2.2 The flap protruding to the separated shear layer denotes high efficiency of the mechanism. 16
2.3 Development of the General Aviation airfoil family [10]. 17
2.4 LS(1) - 0417mod airfoil and its performance at M = 0.15, Re = $4 \cdot 10^6$ and $c_l = 1.0$ [10]. 18
3.1 Input computational geometry. 19
3.2 Example of structured mesh constructed of quadrilateral cells 21
3.3 Example of unstructured mesh with triangular elements. 21
3.4 Hybrid mesh used for validation with quad and tri zone. 22
3.5 Boundary condition distribution. 27
3.6 Example of convergence progress on lift coefficient monitor. 28
3.7 Wall y^+ distribution on different angles of attack. 29
3.8 Boundary layer validation. 29
4.1 Monitored variables of mesh independence study. 32
4.2 Convergence issues. 33
4.3 Validation: lift curve. 34
4.4 Validation: moment curve. 35
4.5 Validation: polar curve. 35
5.1 Geometry of the flapped airfoil. 37
5.2 Detail of mesh generation in the aft part of the airfoil. 39
5.3 Velocity magnitude in pocket region (Contour range is limited for better visualization). 40
5.4 Monitored variables of time-step independence independence study. . 43
5.5 Converged solution. 44
6.1 Phase 1: Contours of mean X-velocity with the minimum value 0.0 in the case F_80_20_40_14. Spoiler-like behaviour of the flap. 46
6.2 Phase 2: Pathlines in the case F_60_40_60_26. 46
6.3 Clipped pressure distribution around the airfoil. Case F_60_40_60_26. Blue represents the area of decreased pressure whereas red indicates higher pressure areas. 47
6.4 Contours of mean X-velocity with the minimum value 0.0 in the case F_80_20_40_26. Decrease of aerodynamic characteristics. 48
6.5 Lift curves of the F_80_20 cases. 49
6.6 Lift curves of the F_70_30 cases. 50

6.7 Lift curves of the F_60_40 cases. 51
7.1 Pressure distribution on the flap. Case F_60_40_60_28. 53
7.2 Elastic flap parameters. Dashed line symbolized predicted deformed shape. 54
7.3 Experimental set-up [27]. 55
7.4 Displacement plot of validation case in Ansys mechanical. 56
7.5 Displacement plot of case study in Ansys mechanical. 57
8.1 Contours of mean X-velocity with the minimum value 0.0 in the case F_60_40_60_28. 59
A.1 Contours of turbulence intensity on different Δt. 76
B.1 Contours of mean X-velocity with the minimum value 0.0 in the case F_60_40_60. 77
C.1 Lift to drag ratio curves of the F_80_20 cases. 79
C.2 Moment curves of the F_80_20 cases. 79
C.3 Lift to drag ratio curves of the F_70_30 cases. 81
C.4 Moment curves of the F_70_30 cases. 81
C.5 Lift to drag ratio curves of the F_60_40 cases. 83
C.6 Moment curves of the F_60_40 cases. 83
D.1 Meshed beam representing the flap in structural analysis. 85

LIST OF TABLES

3.1 Input variables used for calculation. 24
3.2 Solver setting. 25
4.1 Mesh independence study data. 32
5.1 Parameters of studied cases. 38
5.2 Transient simulation settings. 41
5.3 Time-step independence study. 42
6.1 Maximum lift coefficient comparison. 51
8.1 Comparison of aerodynamic characteristics between rigid and elastic flap. 59
A.1 MIS general inputs. 73
A.2 Mesh Independence study: variables values. 73
A.3 Digitalized data from the reference [17]. 74
A.4 Simulation output data for validation. 75
C.1 Data of F_80_20 case. 80
C.2 Data of F_70_30 case. 82
C.3 Data of F_60_40 case. 84

LIST OF APPENDICES

A Mesh Independence Study **73**

B Flow Analysis **77**

C Case Results **79**

C.1 F_80_20 Case 79

C.2 F_70_30 Case 81

C.3 F_60_40 Case 83

D Structural Analysis **85**

A MESH INDEPENDENCE STUDY

	Mesh 1	**Mesh 2**	**Mesh 3**	**Mesh 4**
Cell count (quads) [-]	26 384	26 384	77 644	134 284
Cell count (tri) [-]	34 644	178 254	299 008	925 586
Cell count [-]	61 028	204 638	376 652	1 059 870
Domain radius [m]	20	20	30	40
Max. element size (global) [m]	1	1	1	1
Max. element size (density box) [m]	N/A	0,005	0,005	0,0025
Max. element size (wall) [m]	0,003	0,003	0,002	0,001
Growth ratio [-]	1,3	1,3	1,05	1,025
Min. quality [-]	0,29	0,46	0,52	0,46
Min. skew [-]	0,31	0,43	0,43	0,43

Tab. A.1: MIS general inputs.

	Mesh 1			**Mesh 2**		
AoA [deg]	c_l [-]	c_d [-]	c_m [-]	c_l [-]	c_d [-]	c_m [-]
10	1,4224	0,0228	-0,0753	1,4153	0,0225	-0,0739
12	1,5673	0,0284	-0,0696	1,5553	0,0280	-0,0677
14	1,6625	0,0376	-0,0628	1,6490	0,0372	-0,0608
16	1,7008	0,0547	-0,06072	1,6920	0,0555	-0,0589
	Mesh 3			**Mesh 4**		
AoA [deg]	c_l [-]	c_d [-]	c_m [-]	c_l [-]	c_d [-]	c_m [-]
10	1,4097	0,0232	-0,0729	1,4089	0,0223	-0,0727
12	1,5485	0,0278	-0,0665	1,5487	0,0275	-0,0664
14	1,6413	0,0369	-0,0597	1,6436	0,0368	-0,0599
16	1,6655	0,0532	-0,0532	N/A	N/A	N/A

Tab. A.2: Mesh Independence study: variables values.

NASA					
AoA [deg]	c_l [-]	AoA [deg]	c_m [-]	c_l [-]	c_d [-]
-8,03	-0,52	-8,24	-0,064	-0,53	0,016
-6,00	-0,31	-6,23	-0,070	-0,31	0,013
-4,07	-0,07	-4,23	-0,078	-0,08	0,009
-2,07	0,17	-2,26	-0,086	0,17	0,009
-0,01	0,42	-0,18	-0,087	0,41	0,010
2,02	0,64	1,85	-0,089	0,64	0,011
4,02	0,87	3,82	-0,089	0,86	0,011
6,05	1,10	5,89	-0,090	1,10	0,013
10,07	1,46	9,78	-0,081	1,46	0,017
13,02	1,65	12,78	-0,067	1,64	0,024
14,16	1,69	13,91	-0,065	1,68	0,029
15,01	1,71	14,75	-0,062	1,71	0,034
15,53	1,51	15,31	-0,065		
16,09	1,42	15,85	-0,091		
17,03	1,36	16,81	-0,101		
18,01	1,33	17,86	-0,105		
19,09	1,31	18,92	-0,107		

Tab. A.3: Digitalized data from the reference [17].

FLUENT			
AoA [deg]	c_l [-]	c_d [-]	c_m [-]
-5	-0,1997	0,0133	-0,0691
-4	-0,0820	0,0130	-0,0710
-3	0,0359	0,0128	-0,0729
-2	0,1536	0,0127	-0,0746
-1	0,2707	0,0127	-0,0761
0	0,3867	0,0129	-0,0775
1	0,5019	0,0131	-0,0786
2	0,6154	0,0135	-0,0795
3	0,7271	0,0140	-0,0802
4	0,8364	0,0146	-0,0805
5	0,9432	0,0154	-0,0805
6	1,0466	0,0163	-0,0800
7	1,1459	0,0174	-0,0791
8	1,2402	0,0187	-0,0776
9	1,3287	0,0204	-0,0756
10	1,4102	0,0223	-0,0729
11	1,4836	0,0247	-0,0698
12	1,5477	0,0278	-0,0664
13	1,6009	0,0318	-0,0629
14	1,6407	0,0369	-0,0596
15	1,6656	0,0437	-0,0568
16	1,6649	0,0531	-0,0552

Tab. A.4: Simulation output data for validation.

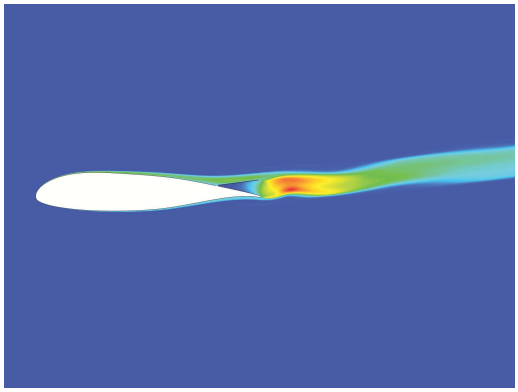

(a) $\Delta t = 0.01$.

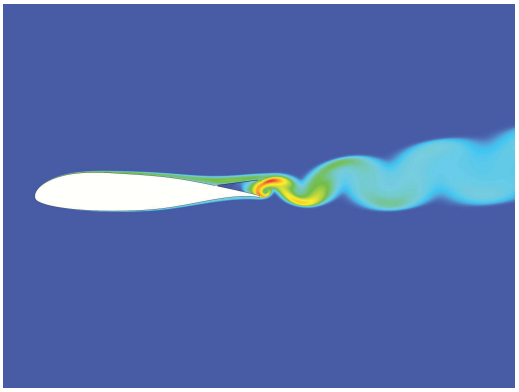

(b) $\Delta t = 0.001$.

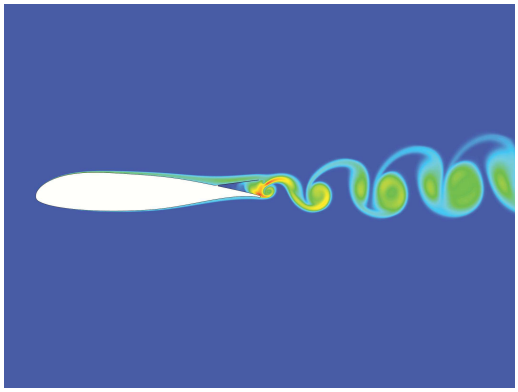

(c) $\Delta t = 0.0001$.

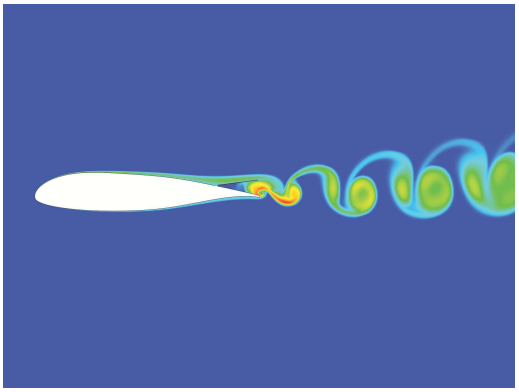

(d) $\Delta t = 0.00001$.

Fig. A.1: Contours of turbulence intensity on different Δt.

B FLOW ANALYSIS

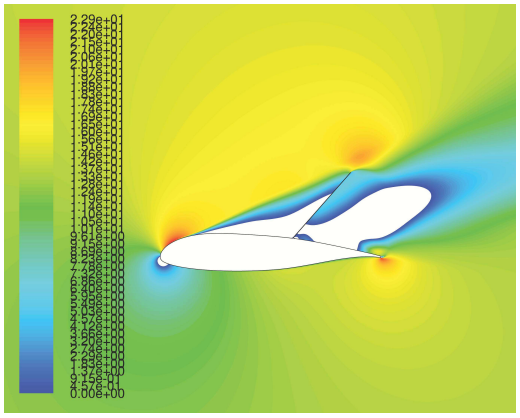

(a) Phase 1 on 22deg of AoA.

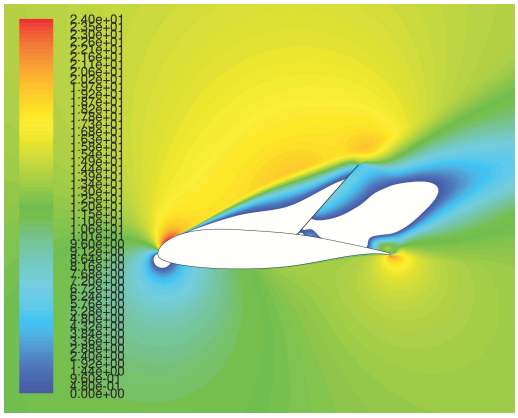

(b) Phase 1-2 on 24deg of AoA.

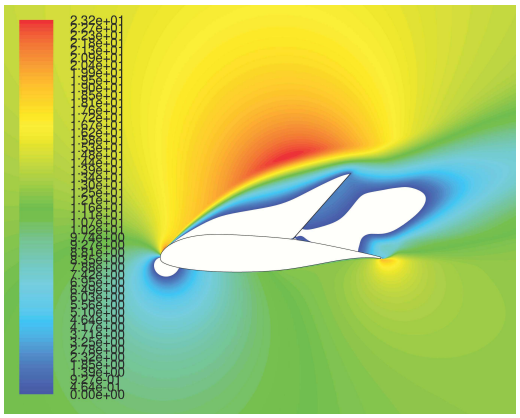

(c) Phase 2 on 26deg of AoA.

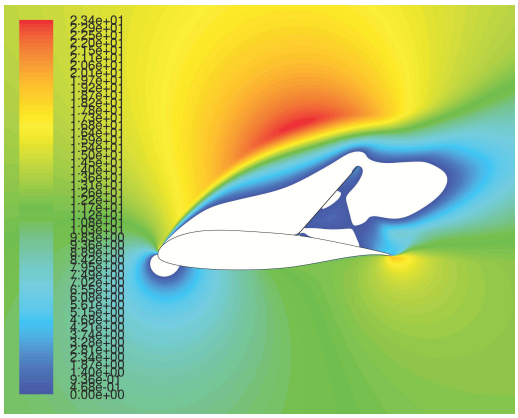

(d) Phase 2-3 on 28deg of AoA.

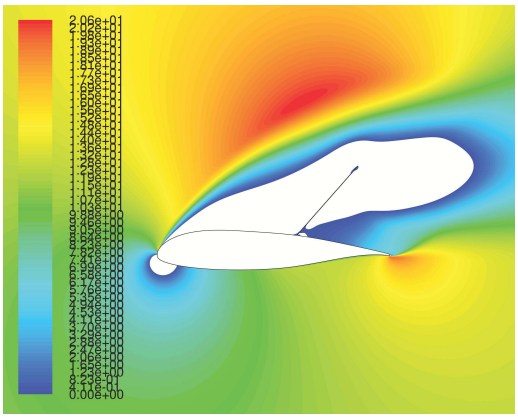

(e) Phase 3 on 30deg of AoA.

Fig. B.1: Contours of mean X-velocity with the minimum value 0.0 in the case F_60_40_60.

C CASE RESULTS

C.1 F_80_20 Case

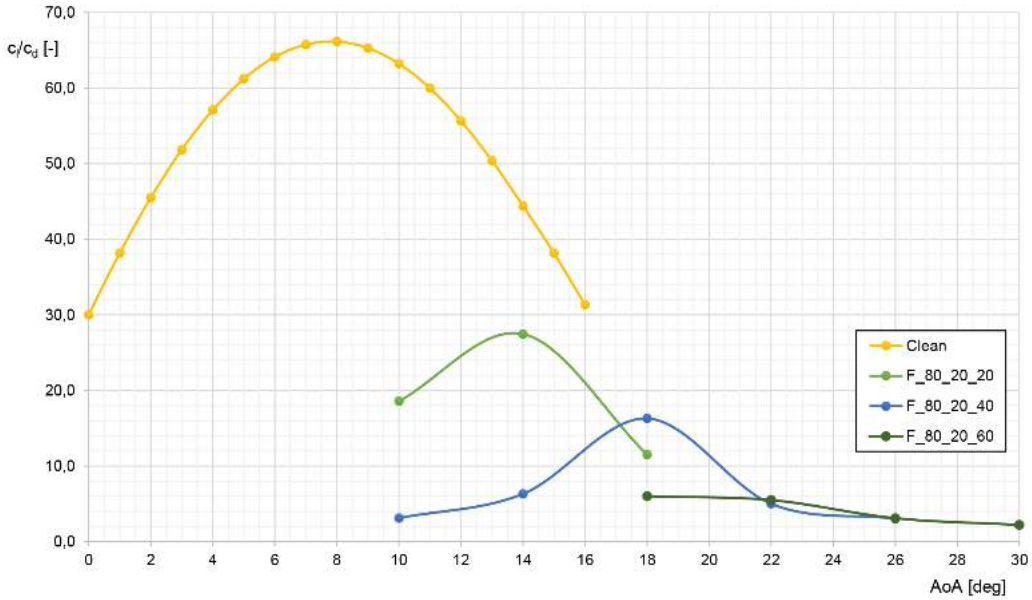

Fig. C.1: Lift to drag ratio curves of the F_80_20 cases.

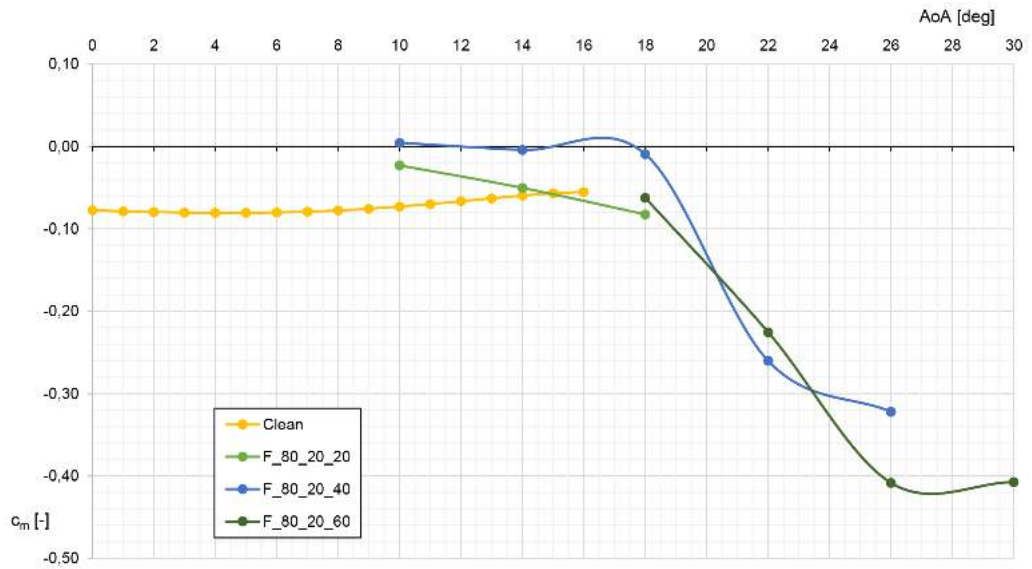

Fig. C.2: Moment curves of the F_80_20 cases.

F_80_20_20				
AoA [deg]	c_l [-]	c_d [-]	c_m [-]	c_l/c_d [-]
10	1.07	0.057	-0.023	18.6
14	1.57	0.057	-0.050	27.5
18	1.36	0.118	-0.082	11.5
F_80_20_40				
AoA [deg]	c_l [-]	c_d [-]	c_m [-]	c_l/c_d [-]
10	0.57	0.182	0.004	3.1
14	1.12	0.178	-0.004	6.3
18	1.56	0.096	-0.009	16.3
22	1.73	0.345	-0.260	5.0
26	1.71	0.562	-0.322	3.0
F_80_20_60				
AoA [deg]	c_l [-]	c_d [-]	c_m [-]	c_l/c_d [-]
18	1.39	0.232	-0.062	6.0
22	1.73	0.315	-0.225	5.5
26	1.96	0.633	-0.408	3.1
30	1.76	0.793	-0.407	2.2

Tab. C.1: Data of F_80_20 case.

C.2 F_70_30 Case

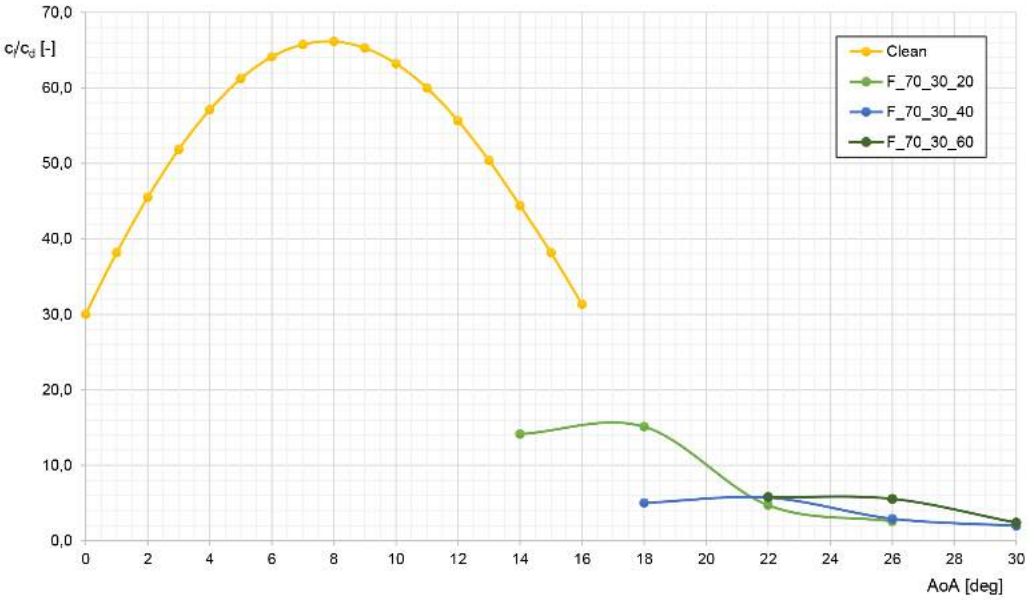

Fig. C.3: Lift to drag ratio curves of the F_70_30 cases.

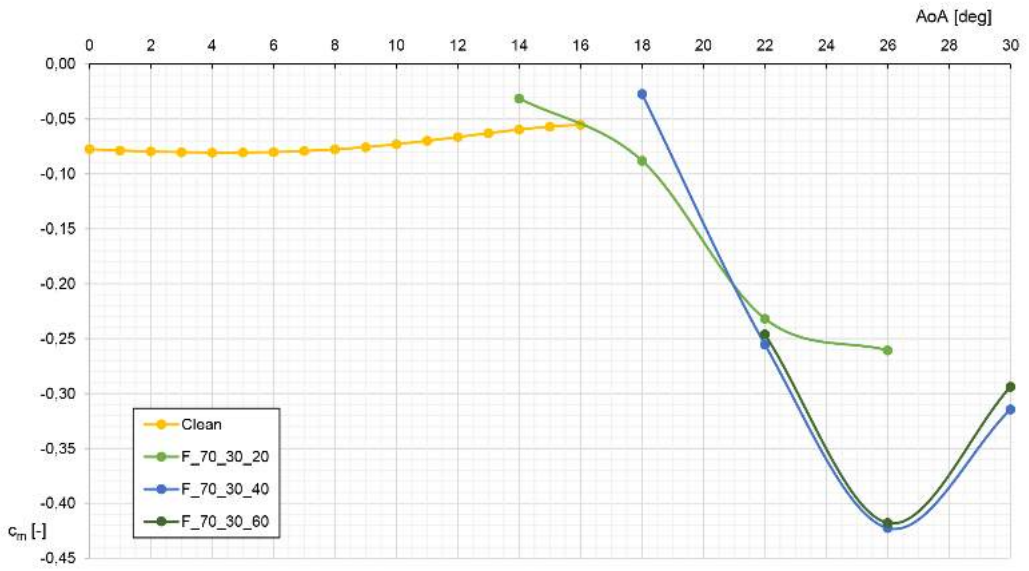

Fig. C.4: Moment curves of the F_70_30 cases.

F_70_30_20				
AoA [deg]	c_l [-]	c_d [-]	c_m [-]	c_l/c_d [-]
14	1.36	0.096	-0.031	14.1
18	1.52	0.101	-0.088	15.1
22	1.61	0.343	-0.232	4.7
26	1.45	0.565	-0.261	2.6
F_70_30_40				
AoA [deg]	c_l [-]	c_d [-]	c_m [-]	c_l/c_d [-]
18	1.27	0.254	-0.027	5.0
22	1.73	0.302	-0.255	5.7
26	1.89	0.649	-0.423	2.9
30	1.44	0.727	-0.314	2.0
F_70_30_60				
AoA [deg]	c_l [-]	c_d [-]	c_m [-]	c_l/c_d [-]
22	1.78	0.307	-0.246	5.8
26	2.06	0.372	-0.418	5.6
30	1.43	0.599	-0.294	2.4

Tab. C.2: Data of F_70_30 case.

C.3 F_60_40 Case

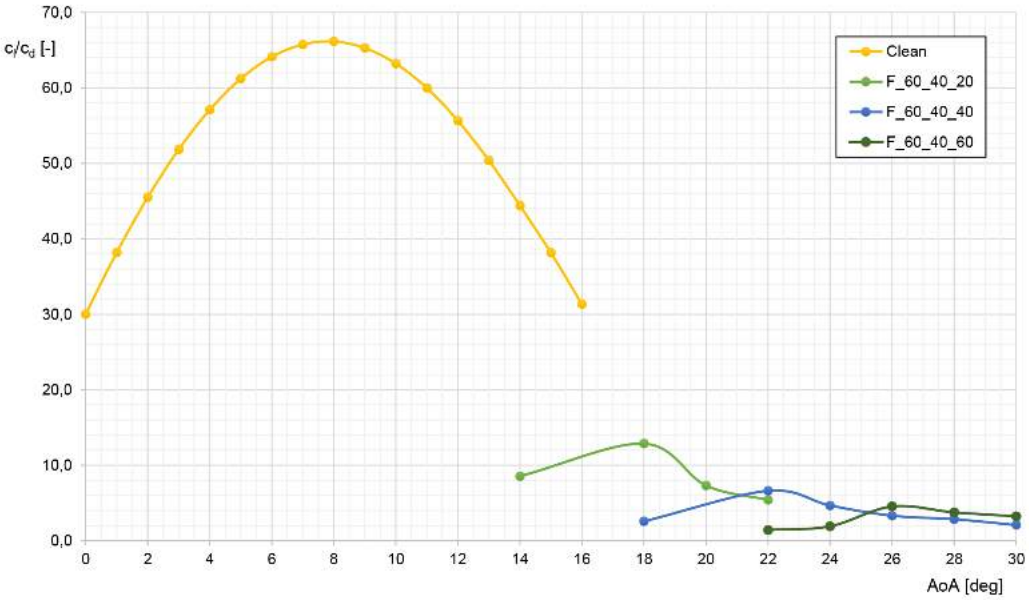

Fig. C.5: Lift to drag ratio curves of the F_60_40 cases.

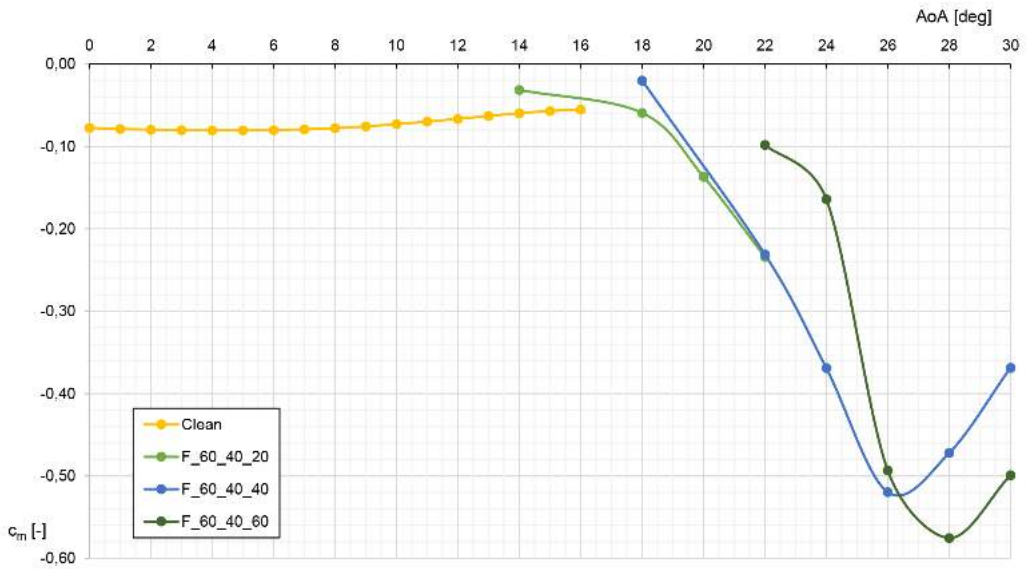

Fig. C.6: Moment curves of the F_60_40 cases.

F_60_40_20				
AoA [deg]	c_l [-]	c_d [-]	c_m [-]	c_l/c_d [-]
14	1.21	0.142	-0.031	8.5
18	1.67	0.130	-0.059	12.9
20	1.38	0.189	-0.137	7.3
22	1.67	0.310	-0.234	5.4
F_60_40_40				
AoA [deg]	c_l [-]	c_d [-]	c_m [-]	c_l/c_d [-]
18	0.97	0.378	-0.020	2.6
22	1.78	0.269	-0.231	6.6
24	1.98	0.423	-0.369	4.7
26	2.20	0.664	-0.520	3.3
28	1.97	0.693	-0.472	2.8
30	1.55	0.742	-0.369	2.1
F_60_40_60				
AoA [deg]	c_l [-]	c_d [-]	c_m [-]	c_l/c_d [-]
22	1.00	0.707	-0.098	1.4
24	1.33	0.695	-0.164	1.9
26	2.32	0.511	-0.493	4.5
28	2.41	0.642	-0.575	3.8
30	2,06	0.637	-0.499	3.2

Tab. C.3: Data of F_60_40 case.

D STRUCTURAL ANALYSIS

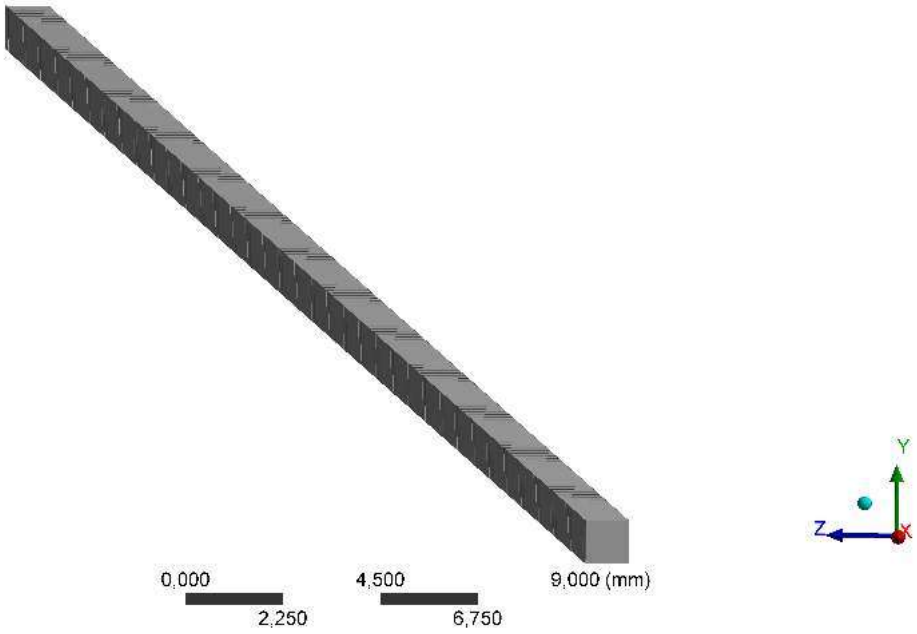

Fig. D.1: Meshed beam representing the flap in structural analysis.